Jimenéz Garcia, A. and Barakos, G.N. (2018) Accurate predictions of rotor hover performance at low and high disc loadings. *Journal of Aircraft*, 55(1), pp. 89-110. (doi:10.2514/1.C034144)

This is the author's final accepted version.

There may be differences between this version and the published version. You are advised to consult the publisher's version if you wish to cite from it.

http://eprints.gla.ac.uk/133234/

Deposited on: 23 December 2016

Enlighten – Research publications by members of the University of Glasgow
http://eprints.gla.ac.uk

Accurate Predictions of Rotor Hover Performance at Low and High Disc Loadings

A. Jimenéz Garcia[a], G.N. Barakos[b]
CFD Laboratory, School of Engineering, University of Glasgow, G12 8QQ Glasgow, UK

This paper presents evidence on the ability of modern CFD methods to accurately predict hover performance of rotors with modest computer resources. The paper uses two well-studied blades, the S-76 main rotor blade and the XV-15 tiltrotor blade. The results are compared with experiments and show that the performance is well predicted. In addition, the employed Computational Fluid Dynamics method was able to capture the effects of the tip Mach number, tip shape, blade aeroelasticity, and flow transition on the performance of the blade as well as on the wake structure and the rotor acoustics.

Nomenclature

$\boldsymbol{R}$	=	flow equation residual vector
$\boldsymbol{W}$	=	flow solution vector
a_∞	=	freestream speed of sound, *m/s*
B	=	tip-loss factor, $1 - \frac{\sqrt{C_T}}{N_b}$
c	=	blade chord, *m*
c_{ref}	=	reference blade chord, *m*
c_e	=	equivalent blade chord, *m*, [Eq. 4]
C_P	=	blade section pressure coefficient, $C_P = \dfrac{P - P_\infty}{1/2\rho_\infty(\Omega r)^2}$
C_P^*	=	critical pressure coefficient
C_Q	=	rotor torque coefficient, $C_Q = \dfrac{Q}{\rho_\infty(\Omega R)^2\pi R^3}$
C_q	=	blade section torque coefficient, $C_q = \dfrac{\mathrm{d}C_Q}{\mathrm{d}\psi}$
C_T	=	rotor thrust coefficient, $C_T = \dfrac{T}{\rho_\infty(\Omega R)^2\pi R^2}$

[a] PhD Student, CFD Laboratory, School of Engineering. Email: a.jimenez-garcia.1@research.gla.ac.uk
[b] Professor, MAIAA, MRAeS, CFD Laboratory, School of Engineering. Email: George.Barakos@glasgow.ac.uk, corresponding author

C_t	=	blade section thrust coefficient, $C_t = \dfrac{\mathrm{d}C_T}{\mathrm{d}\psi}$
C_{DO}	=	overall profile drag coefficient
f	=	integration surface defined by $f = 0$
k	=	turbulent kinetic energy, m^2/s^2
k_i	=	induced power factor
M_{tip}	=	blade-tip Mach number, $M_{\text{tip}} = \dfrac{V_{\text{tip}}}{a_\infty}$
N_b	=	number of blades
P	=	pressure, *Pa*
P_∞	=	freestream pressure, *Pa*
Q	=	rotor torque, $N \cdot m$
R	=	rotor radius, *m*
r	=	radial coordinate along the blade span, *m*
r_H	=	distance from an acoustic probe to the rotor hub, *m*
T	=	rotor thrust, *N*
t	=	blade section aerofoil thickness
T_{ij}	=	Lighthill stress tensor, *Pa*
V_∞	=	freestream velocity, *m/s*
V_{tip}	=	blade-tip speed, $V_{\text{tip}} = \Omega R$, *m/s*
AR	=	aspect ratio, R/c_{ref}
FoM	=	figure of merit, $\text{FoM} = \dfrac{C_T^{3/2}}{\sqrt{2}C_Q}$
Re	=	Reynolds number, $\text{Re} = V_{\text{tip}} c_{\text{ref}}/\nu_\infty$
∞	=	freestream value
ref	=	reference value
tip	=	blade-tip value
β	=	coning angle, *deg*

η	=	propeller propulsive efficiency, $\eta = \dfrac{C_T V_\infty}{C_Q V_{\text{tip}}}$
γ	=	intermittency factor
μ	=	advance ratio, $\mu = \dfrac{V_\infty}{V_{\text{tip}}}$
ν_∞	=	freestream kinematic viscosity, *m/s*^{2}
Ω	=	rotor rotational speed, *rad/s*
Ψ	=	local azimuth angle, *deg*
ψ	=	normalised radial coordinate along the blade span, $\psi = r/R$
ρ	=	density, *kg/m*^{3}
ρ_∞	=	freestream density, *kg/m*^{3}
σ	=	rotor solidity, $\sigma = \dfrac{N_b c_{\text{ref}}}{\pi R}$
Θ	=	local blade twist angle, *deg*
θ_{75}	=	blade pitch angle at $r/R = 0.75$, *deg*
ALE	=	arbitrary lagrangian eulerian
BEL	=	blade element theory
BILU	=	block incomplete lower-upper
BMTR	=	basic model test ring
CFD	=	computational fluid dynamics
CFL	=	Courant-Friedrichs-Lewy condition
CSD	=	computational structural dynamics
DDES	=	delay-detached-eddy simulation
DES	=	detached eddy simulation
HELIOS	=	helicopter overset simulations
HFWH	=	helicopter Ffowcs Williams-Hawkings
HMB	=	helicopter multi-block
IGE	=	in-ground effect

ISA	=	international standard atmosphere
LES	=	large eddy simulation
NFAC	=	AMES national full-scale aerodynamics complex
OGE	=	out-of-ground effect
SST	=	shear-stress transport

I. Introduction

Recently, significant progress has been made in accurately predicting the efficiency of hovering rotors using Computational Fluid Dynamics (CFD) [1]. The hover condition is an important design point due to its high power consumption. Consequently, accurate prediction of the rotor figure of merit (FoM) along with the strength and position of the vortex core is of practical interest to rotorcraft manufacturers.

Over the years, various approaches have been developed for modelling rotors in hover. The simplest models are based on one-dimensional momentum theory and Blade Element Theory (BET) [2], which do not account for non-ideal flow, viscous losses, and swirl flow loss effects. Hence, the vortex wake of the rotor is not accurately represented for this basic model. Alternatively, prescribed and free-wake approaches have a detailed vortex wake due to the representation of the root and tip vortices, but they still need additional data for the blade loads. More recently, high fidelity approaches based on numerical simulation of the Navier-Stokes equations are being gradually employed partly due to the emergence of parallel clusters, reducing the high computational time associated with these approaches, and progress with accuracy and stability of CFD solvers.

During the eighties, a comprehensive experimental study of four model-scale rotors (UH-60A, S-76, High Solidity, and H-34) in hover, was conducted by Balch [3, 4]. Further work by Balch and Lombardi [5, 6] compared advanced tip configurations for the UH-60A and S-76 rotor blade geometries, again in hover. The Balch and Lombardi S-76 rotor blade was of 1/4.71 scale while the Balch S-76 rotor blade was of 1/5 scale. The effect of using different tip configurations (rectangular, swept, tapered, swept-tapered, and swept-tapered with anhedral) on the performance of the rotors was experimentally investigated in-ground effect (IGE) and out-of-ground effect (OGE) conditions. This study was conducted at the Sikorsky Model Hover Test Facility using the Basic Model Test Ring (BMTR).

To assess the accuracy of the present method in predicting the figure of merit at high disc loading, the XV-15 tiltrotor blade was also considered. Very little wind tunnel data is available for model and full-scale tiltrotors. At the early stage of the XV-15 program, the NASA 40-by-80-Foot Wind Tunnel was used to measure integrated rotor loads in helicopter [7], aeroplane and transition-corridor modes [8]. However, force and moment measurements did not exclude the contribution from the airframe. The NASA-Ames Outdoor Aeronautical Research Facility (OARF) was also extensively used by Felker *et al.*[9] with the XV-15 rotor and Bartie *et al.*[10] with the XV-15 Advanced Technology Blade (ATB). The hover and forward flight tests

began in the late 90s with the work of Light [11] in the 80-ft by 120-ft wind tunnel at NASA Ames, but only few conditions were tested. To fill this gap, Betzina [12] in 2002 undertook an extensive campaign of experiments on the full-scale XV-15 rotor, where the experiments were corrected for hub and tares effects. For all sets of experiments cited, neither surface pressure nor skin friction coefficients were measured. In this regard, Wadcook *et al.*[13] measured skin friction coefficients on a hovering full-scale XV-15 tiltrotor in the 80-ft by 120-ft wind tunnel at NASA Ames. At low thrust, a region of laminar flow was encountered over a significant fraction of the blade chord, while at high disc loading conditions, the laminar to turbulent transition region on the upper blade surface moved towards the blade leading edge with a fully turbulent boundary layer encountered outboard. This set of experiments can be used to validate and improve flow transition models for tiltrotors.

As a means of evaluating the current state-of-the-art performance prediction using different CFD solvers and methods for the same blade geometry, the AIAA Applied Aerodynamics Rotor Simulations Working Group [14, 15] was established in 2014. The 1/4.71 scale S-76 rotor blade [5, 6] was selected for assessment because of its public availability and data set with various tip shapes. Sheng [16] used the unstructured Navier-Stokes CFD solver U^2NCLE to perform simulations on the 1/4.71 scale S-76 rotor blade. The effect of transition models such as the local correlation-based transition models by Langtry [17, 18], as well as the Stall Delay Model (SDM) were investigated. Likewise, Jain [19] evaluated the performance of the S-76 model-scale rotor with swept-tapered tip using the HPCMP CREATE^{TM}-AV HELIOS (Helicopter Overset Simulations) CFD solver, where the FoM was predicted within 1 count. The same rotor blade was assessed using the OVERFLOW structured module of HELIOS by Narducci [20, 21]. The results obtained with the structured grid method were consistent with the one performed with the unstructured grid method by Tadghighi [22], showing also an under-predicted figure of merit. Despite that the figure of merit was difficult to converge, the performance sensitivities to the tip Mach number and tip shape were well predicted.

Concerning numerical simulations of the XV-15 tiltrotor blade, Kaul *et al.*[23, 24] studied the effect of inflow boundary conditions and turbulent models on the hovering XV-15 rotor blade, using the OVERFLOW2 CFD solver. Results with the Spalart-Allmaras model [25] with the Detached Eddy Simulation formulation, revealed lack of agreement with the experiments of Wadcook *et al.*[13] in the laminar-turbulent transitional region. Likewise, Yoon *et al.*[26] investigated the effect of the employed turbulence model on the hover performance, and skin friction coefficients of the XV-15 rotor blade at a collective of $10°$. It was found that the k-ω SST-DDES turbulence model predicted the figure of merit closer to experiment that the SA-DDES one-equation model. However, minimal differences between these fully-turbulent models were observed in the predictions of skin friction coefficient, which did not reproduce well the flowfield encountered in the experiment [13]. Sheng *et al.*[27] used the U^2NCLE and HELIOS CFD solvers to assess the effect of transition models in predicting the hover figure of merit on the XV-15 blade. Despite the use of a massive grid of 294 million cells for the whole rotor, results at $10°$ collective showed an over-predicted FoM with a discrepancy of more than 3%. It was shown that the transitional flow modelling did not have a significant impact on the predicted FoM mainly due to the small laminar-turbulent transition region encountered

on the XV-15 blades. A detailed performance analysis of the hover and propeller modes of the XV-15 blades were performed by Gates [28] using the HMB CFD solver. Good agreement with published experimental data was reported, even though a medium grid size (9.6 million cells per blade) was employed for computations. Furthermore, the effect of the hub spinner on the propeller performance at moderate advance ratios was highlighted.

In this work, we present an aerodynamic study of two well-studied rotors, the S-76 helicopter rotor and the XV-15 tiltrotor, with high-fidelity computational fluid dynamics. The aim is to assess the level of accuracy of the present CFD method in predicting the figure of merit for a hover cases with modest computer resources. This is addressed by comparing with experimental data available in the literature [5, 6, 9, 11, 12]. To reduce the computational cost, we solved the hover flow by casting the equations as a steady-state problem in a noninertial reference frame. The first part of this paper is devoted on the performance of the 1/4.71 scale S-76 rotor in hover. The effect of various tip shapes for a wide range of collective pitch settings and tip Mach numbers is evaluated. In addition, an aeroacoustic study using the Helicopter Ffowcs Williams-Hawkings (HFWH) code, is undertaken to assess the different tip shapes on the model-scale S-76. In addition, hovering simulations for full-scale S-76 are compared with wind tunnel data in terms of FoM. The effect of aeroelastic deformation of the blades is investigated through a loose coupling CFD/CSD method. The second part of this paper presents performance analysis of the XV-15 tiltrotor blade. Results are presented for a range of design points, which includes medium and high thrust hover conditions. The impact of a fully-turbulent k-ω SST and transitional k-ω SST-γ models on the predicted figure of merit is also shown at collective angles of 3° and 10°. The ability of those models in predicting the experimental skin friction distribution [13] on the blade surface is also discussed.

II. HMB Solver

The Helicopter Multi-Block (HMB) [29–32] code is used as the CFD solver for the present work. It solves the Unsteady Reynolds Averaged Navier-Stokes (URANS) equations in integral form using the arbitrary Lagrangian Eulerian (ALE) formulation, first proposed by Hirt *et al.*[33], for the time-dependent domains, which may include moving boundaries. The Navier-Stokes equations are discretised using a cell-centred finite volume approach on a multi-block grid. The spatial discretisation of these equations leads to a set of ordinary differential equations in time,

$$\frac{d}{dt}(\boldsymbol{W}V) = -\boldsymbol{R}(\boldsymbol{W}), \tag{1}$$

where $\boldsymbol{W}$ and $\boldsymbol{R}$ are the flow solution and flux residual vectors, respectively, and V is the volume of the cell. To evaluate the convective fluxes, Osher [34] and Roe [35] approximate Riemann solvers are used in HMB, while the viscous terms are discretised using a second order central differencing spatial discretisation. The Monotone Upstream-centred Schemes for Conservation Laws (MUSCL) developed by van Leer [36] is used to provide third order accuracy in space. The HMB solver uses the alternative form of the Albada limiter [37] being activated in regions where a large gradients are encountered, mainly due to shock waves, avoiding the non-physical spurious oscillations. An implicit, dual-time stepping method is employed to performed

the temporal integration. The solution is marching in the pseudo-time to achieve fast convergence, using a first-order backward difference. The linearised system of the Navier-Stokes equations is solved using the Generalised Conjugate Gradient method with a Block Incomplete Lower-Upper (BILU) factorisation as a pre-conditioner [38]. Multi-block structured meshes are used for HMB, which allow easy sharing of the calculation load in parallel computing. Structured multi-block hexa meshes are generated using ICEM-Hexa™.

A. Turbulence and Transition Models

Various turbulence models are available in HMB, including several one-equation, two-equation, three-equation, and four-equation turbulence models. Furthermore, Large-Eddy Simulation (LES), Detached-Eddy Simulation (DES), and Delay-Detached-Eddy Simulation (DDES) are also available. For this study, two and three equations models were employed using the fully-turbulent k-ω SST and the transitional model k-ω SST-γ both from Menter [39, 40]. It is well known that the fully-turbulent k-ω SST model predicts the transition onset further upstream than nature, requiring the use of transition models. In this regard, Menter *et al.*[41] developed a model for the prediction of laminar-turbulent transitional flows, involving two transport equations for the intermittency factor γ and the momentum thickness Reynolds number Re_θ. The intermittency factor γ is used to trigger and control the transition onset location, and it varies between 0 (laminar flow) to 1 (fully-turbulent flow). In 2015, a new one-equation local correlation-based transition model γ was proposed by Menter *et al.*[40], where the Re_θ equation was avoided. The form of the transport equation for the intermittency factor γ reads as:

$$\frac{\partial(\rho\gamma)}{\partial t} + \frac{\partial(\rho U_j \gamma)}{\partial x_j} = P_\gamma - E_\gamma + \frac{\partial}{\partial x_j}\left[\left(\mu + \frac{\mu_t}{\sigma_\gamma}\right)\frac{\partial \gamma}{\partial x_j}\right] \tag{2}$$

where P_γ and E_γ represent the production and destruction sources respectively. A more detailed description of the γ equation can be found in [40].

III. S-76 Scale-Model Rotor Blade

A. S-76 Rotor Geometry

This work begins by considering the four-bladed S-76 model rotor, of 1/4.71 scale, which features -10° of linear twist. The main characteristics of the model rotor blades are summarised in Table 1. The blade planform has been generated using eight radial stations, varying the twist Θ along the span of blade defined with zero collective pitch at the 75% R. The SC-1013-R8 aerofoil is used from the root of the blade up to 18.9% R, the SC-1095-R8 aerofoil is used from 40% R to 80% R, and the SC-1095 aerofoil is used from 84% R to the tip. Between aerofoils, a linear transition zone was used. To increase the maximum rotor thrust, a cambered nose droop section was added to the SC-1095. Adding droop at the leading edge had two effects: it extended the SC-1095 chord, and reduced the aerofoil thickness from 9.5 to 9.4 percent. This section was designated as the SC-1095-R8. A detailed comparison and the aerodynamic characteristics of these aerofoils can be found in Bousman [42]. The planform of the S-76 model rotor with 60% taper and 35° swept tip, the

details on the blade radial twist, and the chord distributions are shown in Figure 1. The thickness-to-chord ratio (t/c) is held constant, and extends to almost 60% of the blade.

Table 1: Geometric properties of the 1/4.71 scale S-76 rotor [5].

Parameter	Value
Number of blades, N_b	4
Rotor radius, R	1.42 *m* (56.04 *in*)
Reference blade chord, c_{ref}	0.0787 *m* (3.1 *in*)
Aspect ratio, R/c_{ref}	18.07
Rotor solidity, σ	0.0704
Linear twist angle, Θ	-10°

The three blade tips considered for simulations were: rectangular, 60% taper-35° swept (baseline), and 60% taper-35° swept-20° anhedral. Flat and rounded tip-caps were also considered to study the effect of the tip vortex on the hover efficiency. Considering the rounded tip, two steps were taken to generate a smooth tip-cap surface. First, a small part of the blade was cut off at 1/2 of the maximum t/c (which is 9.5%) of the tip aerofoil. After this, the upper and lower points of the aerofoil were revolved about each midpoint of the section. Following this procedure, the radius of the blade did not suffer a significant modification, changing originally from 56.04 to 56.03 inches. Figure 2 shows a view of the S-76 model rotor with 60% taper-35° swept-20° anhedral with (a) flat and (b) rounded tip-caps installed. The 20 degrees of anhedral were introduced following the report of Balch and Lombardi [5] (Figure 9, page 45). Participants of the AIAA hover workshop considered an anhedral angle of 16.234 degrees according to an internal report of Sikorsky Aircraft Corporation. In this work we follow Balch and Lombardi [5] but also computed a case with 16.234 degrees of anhedral (Figure 3).

B. S-76 Rotor Mesh

As the S-76 is a four-bladed rotor, only a quarter of the domain was meshed, assuming periodic conditions for the flow in the azimuthal direction (see Figure 4 (a)). If the wake generated by the rotor is assumed to be steady, the hover configuration can be seen as a steady problem. A C-topology around the leading edge of the blade was selected, whereas an H-topology was employed at the trailing edge of the blade (see Figure 4 (b)). This configuration permits an optimal resolution of the boundary layer due to the orthogonality of the cells around the blade surface. Table 2 lists the grids employed for this study, showing the main meshing parameters and point distributions over the blade surface.

The first cell normal to the blade was set to $7.87 \cdot 10^{-7} m$ $(1.0 \cdot 10^{-5} c_{\text{ref}})$ and $3.96 \cdot 10^{-6} m$ $(5.0 \cdot 10^{-5} c_{\text{ref}})$ for the chimera and matched grids, respectively, which assures y^+ less than 1.0 everywhere on the blade for the employed Re. In the chordwise direction, between 235-238 mesh points were used, whereas in the spanwise direction 216 mesh points were used. A blunt trailing-edge was modelled using 42 mesh points. A C-H multi-block topology was used around the S-76 model rotor, combined with a background mesh

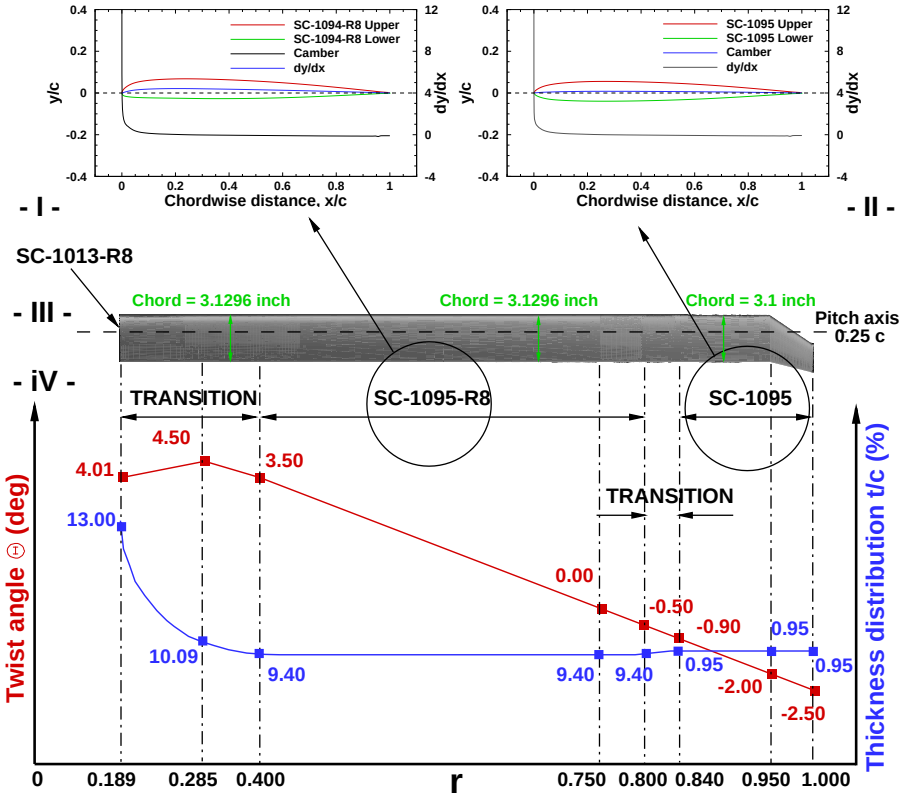

Fig. 1: Geometry of the S-76 model rotor with 60% taper and 35° swept tip, (I) SC-1094-R8 aerofoil, (II) SC-1095 aerofoil, (III) Planform of the S-76 rotor, and (IV) Twist and thickness distributions [3].

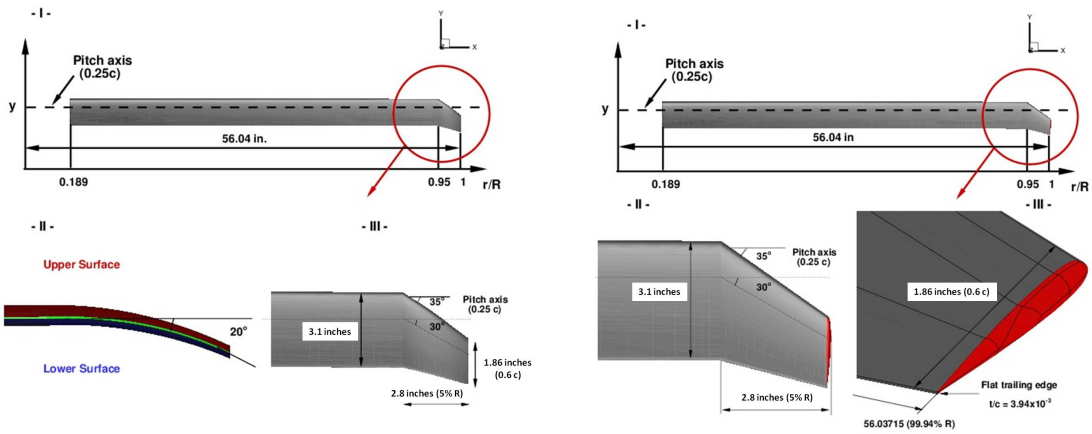

(a) Geometric details of the anhedral flat tip-cap.

(b) Geometric details of the anhedral rounded tip-cap.

Fig. 2: Planform of the S-76 model rotor with 60% taper-35° swept-20° anhedral tip, and geometric details of the flat/rounded tip-caps.

using the chimera method. For all cases, the position of the farfield boundary was extended to $3R$ (above) and $6R$ (below and radial) from the rotor plane, which assures an independent solution with the boundary

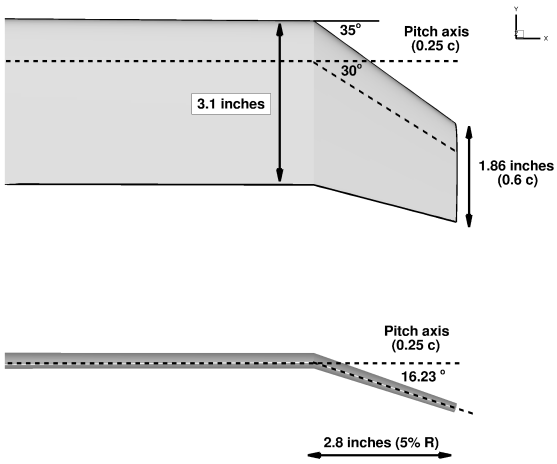

Fig. 3: Planform of the S-76 model rotor with 60% taper-35° swept-16.234^o anhedral tip.

Table 2: Meshing parameters for the S-76 mesh rotor blade.

Grid	Type	Background mesh size	Blade mesh size	Overall mesh size	Variation mesh size	Wall distance
I	Chimera	2 M	3 M	5 M	-	$1.0 \cdot 10^{-5} c_{\text{ref}}$
II	Chimera	3.5 M	4 M	7.5 M	50%	$1.0 \cdot 10^{-5} c_{\text{ref}}$
III	Chimera	3.5 M	26.5 M	30 M	500%	$1.0 \cdot 10^{-5} c_{\text{ref}}$
IV	Matched	-	-	9 M	80%	$5.0 \cdot 10^{-5} c_{\text{ref}}$

M=Million cells.

conditions employed. The rotor hub was modelled as a cylinder, extending from inflow to outflow with a radius corresponding to 2.75% of the rotor radius R. If the chimera method is employed, a cylindrical mesh with nearly uniform spacing in the azimuthal direction is used as background. In the radial and vertical directions, a non-uniform spacing is used to have a finer mesh close to the wake region with a cell spacing of $0.05c_{\text{ref}}$, and coarser mesh towards the external boundaries.

C. Test Conditions and Computations

Table 3 summarises the employed conditions and the computations performed for each tip configuration. The blade-tip Mach number was set to 0.55, 0.60, and 0.65 and a wide range of blade collective angles were considered, corresponding to low, medium, and high thrust. The Reynolds number, based on the reference blade chord of 3.1 inches and on the tip speed, was $1 \cdot 10^6$, $1.09 \cdot 10^6$, and $1.18 \cdot 10^6$, respectively. The S-76 swept-tapered tip with 16.234 degrees of anhedral was compared with results of 20 degrees of anhedral at blade-tip Mach number of 0.60 and at blade collective angle of 9.5 degrees.

All flow solutions were computed by solving the RANS equations, coupled with Menter's k-ω SST turbulence model [39]. The flow equations were integrated with the implicit dual-time stepping method of

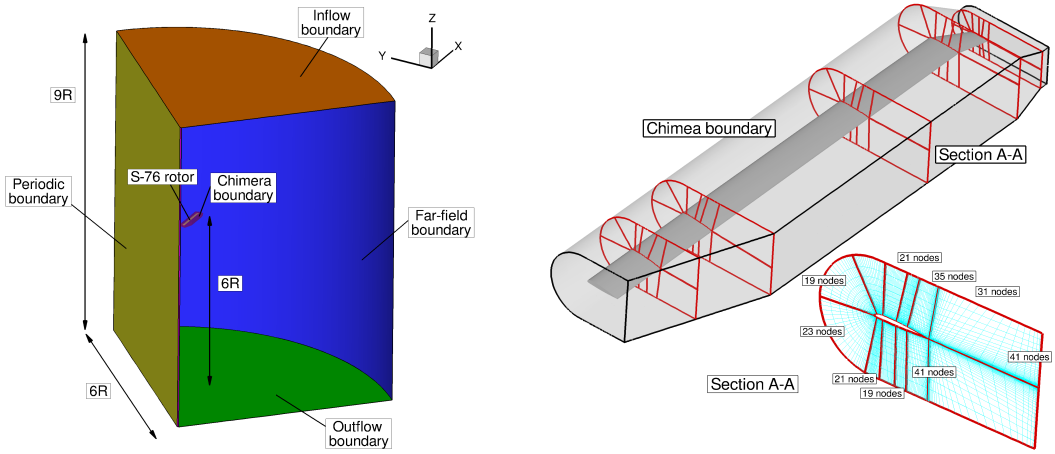

(a) Computational domain.

(b) S-76 rotor mesh.

Fig. 4: Computational domain and boundary conditions employed (left) and detailed view of the S-76 rotor mesh (right).

HMB, using a pseudo-time Courant–Friedrichs–Lewy (CFL) equal to 1.

Table 3: Computational cases for the 1/4.71 scale S-76 rotor.

Tip Geometry	**Grid Employed**	$\mathbf{M}_{\text{tip}}$	θ_{75} (*deg*)
ST-F	I	0.65	6.5,7.5,9.5
ST-F	II	0.65	6.5,7.5,9.5
ST-RD	II	0.65	7.5
ST-F	II	0.65	4-11
ST-F	III	0.65	7
ST-F	IV	0.65	7
ST-F	II	0.60	6-9
ST-F	II	0.55	6-9
R-F	II	0.65	4-9
R-F	II	0.60	6.5,7.5,8.5,9.5
R-RD	II	0.60	7.5
STA-F	II	0.65	6.5,7.5,8.5,9.5
STA-RD	II	0.65	7.5
STA-F	II	0.60	6.5,7.5,9.5,10.5
STA-F^a	II	0.60	9.5

R=Rectangular; ST=Swept-Taper; STA=Swept-Taper-Anhedral; F=flat tip-caps; RD=rounded tip-caps; a=16.234 degrees of anhedral

D. Swept-Taper Tip (Blade-Tip Mach Number of 0.65)

1. Mesh Convergence

The effect of the mesh density on the figure of merit as a function of the blade loading coefficient C_T/σ is shown in Figure 5, where the overset grids I and II (see Table 2) were employed. Vertical lines labelled as empty (3,177 kg) and maximum gross (5,307 kg) weight, define the hovering range of the S-76 helicopter rotor. For the body-fitted mesh, refinements of the boundary layer and surface tip region were carried out. However, the capability to resolve the vortex structure at the background level is key for accurate predictions of the loading on the blade. Hence, half million cells were added to the new background mesh (grid II on Table 2). Consequently, the finest mesh (dashed lines with triangles) shows a better agreement at low, medium, and high thrust coefficients with the test data of Balch and Lombardi [5] (opened squares). Table 4 reports the effect of the mesh density on C_T/σ, C_Q/σ, and FoM for the coarse and medium chimera grids, at blade collective angles θ_{75} of $6.5°$, $7.5°$, and $9.5°$. Even though the thrust coefficient was not trimmed, less than 1% discrepancy was found between the employed grids. This encourages the use of the 7.5 million cells mesh (grid II) to investigate the effect of the tip Mach number for each tip configuration.

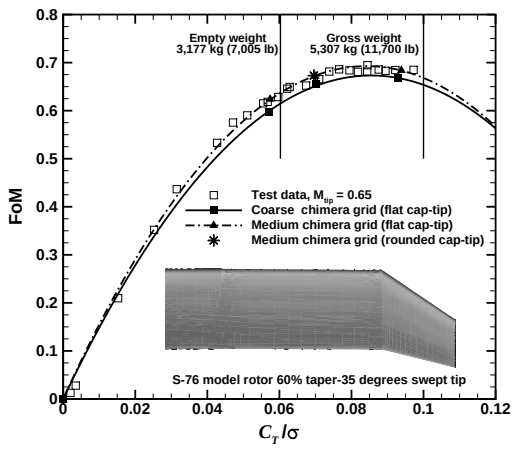

Fig. 5: Effect of the mesh density on the FoM as a function of the C_T/σ for the S-76 model rotor with 60% taper-$35°$ swept tip.

The effect of using rounded tip-caps on the hover efficiency was also investigated, where the medium chimera grid was selected for computations at collective pitch angle of $7.5°$. Comparisons between the rounded (star symbols) and the flat tip-caps (triangle symbols) show a weak effect on the loading of the blade (Figure 5). If the flat tip-caps are taken as reference, differences of -0.5%, -1.0%, and 0.2% in C_T/σ, C_Q/σ, and FoM were found when the rounded tip-caps were used.

Table 4: Effect of the mesh density on the C_T/σ, C_Q/σ, and FoM using the coarse and the medium chimera grids.

Collective	**Coarse chimera grid**			**Medium chimera grid**		
θ_{75} (deg)	$\mathbf{C_T}/\sigma$	$\mathbf{C_Q}/\sigma$	**FoM**	$\mathbf{C_T}/\sigma$	$\mathbf{C_Q}/\sigma$	**FoM**
6.50	0.0570	0.00428	0.596	0.0574	0.00413	0.624
7.50	0.0703	0.00533	0.655	0.0699	0.00516	0.672
9.50	0.0928	0.00794	0.667	0.0939	0.00788	0.684

2. *Integrated Loads*

As shown in Figure 5, the performance of the S-76 with swept and taper tip is well predicted with the medium chimera grid, which has 7.5 million cells per blade. Taking as baseline this tip configuration, the capability of the HMB solver can be explored. In this regard, performance analyses of the S-76 blade for a large range of collective pitch angles using chimera and matched grids are presented. Figure 6 shows the variation of the figure of merit with the blade loading coefficient, at eight collective angles, which cover low, medium, and high thrust. Comparison with experimental data (opened squares) and momentum-based estimates of the figure of merit (dashed lines) are also included. For the momentum-theory curve, an induced power factor k_i of 1.1 and overall profile drag coefficient C_{D0} of 0.01 were selected, showing a wrong tendency of the power divergence at high trust mainly due to flow separation [43]. It can be seen that the CFD computations corresponding to the medium chimera grid (lines with square symbols), are in close agreement with the experimental data. Note that at low thrust, experiments and predictions show low values of the figure of merit, as consequence of the high contribution of the profile drag. The effect of a finer chimera grid (triangles) and a matched grid (stars) (grids III and IV on Table 2, respectively) on the hover performance of the S-76 rotor blade was also investigated at a collective pitch angle of 7°. The solution using the finest chimera grid shows a slight effect on the figure of merit with respect to the computation on the medium one. This supports the selection of the medium chimera grid to evaluate the entire range of collective pitch angles at a reduced computational cost. In addition, the effect of using a matched grid is also reported in Figure 6, showing a mild effect on the loads.

Table 5 summarises the S-76 (baseline) hover performance at a collective pitch of 7° using different grids and methods. The figure of merit performed by the medium chimera grid is predicted to within 0.6 counts, whereas matched and fine chimera grid predicted to within 0.7 and 0.02 counts, respectively.

3. *Sectional Loads*

Figure 7 shows the distribution of sectional thrust and torque coefficients along the rotor radius, for collective pitch angles from 4° to 11°. Both coefficients are normalised with the rotor solidity σ. The influence of the tip vortex on the tip region (from 95% R 100% R) is visible in terms of loading and torque

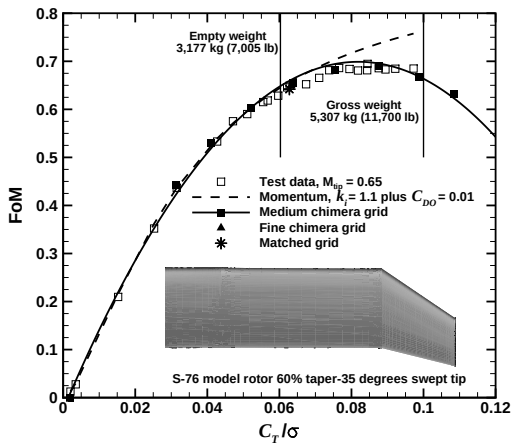

Fig. 6: Figure of merit versus blade loading coefficient for the S-76 model rotor with 60% taper-35° swept tip.

Table 5: Comparison between experimental data [5, 6] and CFD predictions for the 1/4.71 scale S-76 rotor at blade-tip Mach number of 0.65.

Case	Grid	C_T/σ	C_Q/σ	FoM	ΔFoM[%]
Test data, $\theta_{75} = 7.1°$	-	0.06285	0.004553	0.6494	-
Medium chimera grid	II	0.06381	0.004615	0.6551	0.87
Fine chimera grid	III	0.06324	0.004594	0.6496	0.02
Matched grid	IV	0.06278	0.004598	0.6420	1.14

coefficients. As a means of comparing the effect of the thrust coefficient on the tip-loss, a tip-loss factor B is computed. Tip-loss factors $B \approx 1 - \frac{\sqrt{C_T}}{N_b}$ for the lower and higher thrust coefficient (θ_{75} = 4° and 11°) were 0.988 and 0.978, respectively.

4. *Surface Pressure Predictions*

The surface pressure coefficient is analysed for four collective pitch angles at two radial stations along the S-76 blade on the medium chimera grid. It is computed based on the local velocity at each radial station:

$$C_P = \frac{P - P_\infty}{1/2\rho_\infty(\Omega r)^2}. \tag{3}$$

Figure 8 shows the surface pressure coefficient at outboard (r/R = 0.95 and 0.975) blade sections, where the critical C_P^* is also given to asses the sonic region of the blade (local flow above Mach number 1). Both sections reach sonic conditions above rotor collective angles of 7 and 5 degrees, respectively, which lead to increased drag coefficient. This zone is clearly extended further along the blade span as the collective is increased. Despite the use of the swept tip, a mild shock is found at the vicinity of the tip. Figure 9 (a) shows contours of Mach number on a plane extracted at r/R = 0.975 for a blade collective angle of 7.0 degrees,

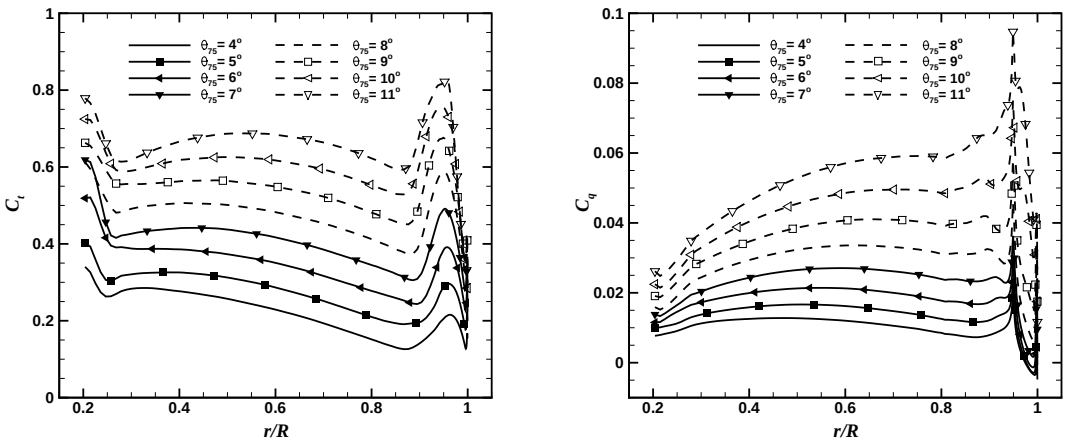

(a) Thrust coefficient.

(b) Torque coefficient.

Fig. 7: Blade section thrust coefficient (left) and torque coefficient (right) for the S-76 blade.

which reveals a weak shock wave. Moreover, Figure 9 (b) shows for each blade collective angle the radial location where the local flow becomes supersonic.

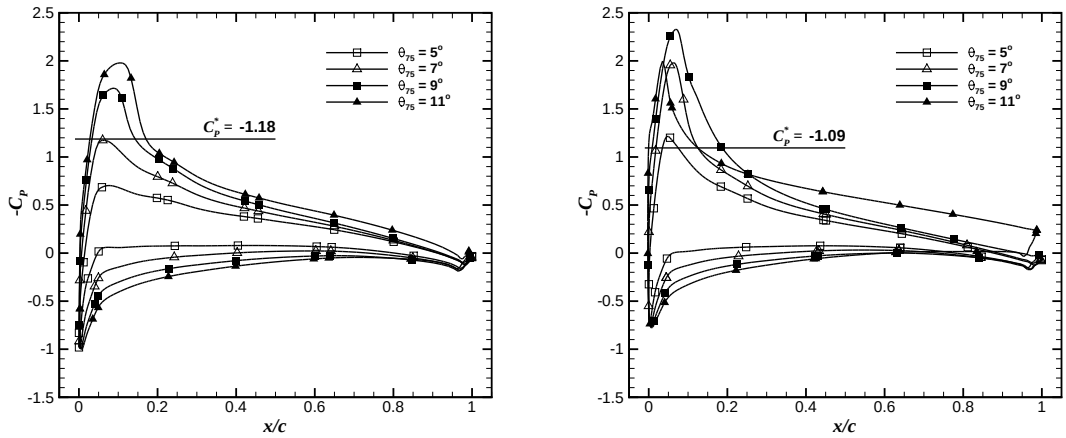

(a) $r/R = 0.95$.

(b) $r/R = 0.975$.

Fig. 8: Surface pressure coefficient for the S-76 blade.

5. *Trajectory and Size of the Tip Vortex*

To ensure realistic predictions of the wake-induced effects, the radial and vertical displacements, and size of the vortex core should be resolved, at least for the first and second wake passages. Figure 10 (a) shows a comparison of the radial and vertical displacements of the tip vortices, as functions of the wake age (in degrees), with the prescribed wake-models of Kocurek [44] and Landgrebe [45]. It should be mentioned that, a blade loading coefficient C_T/σ = 0.0638 was selected, which corresponds to θ_{75} = 7.0°. Both empirical

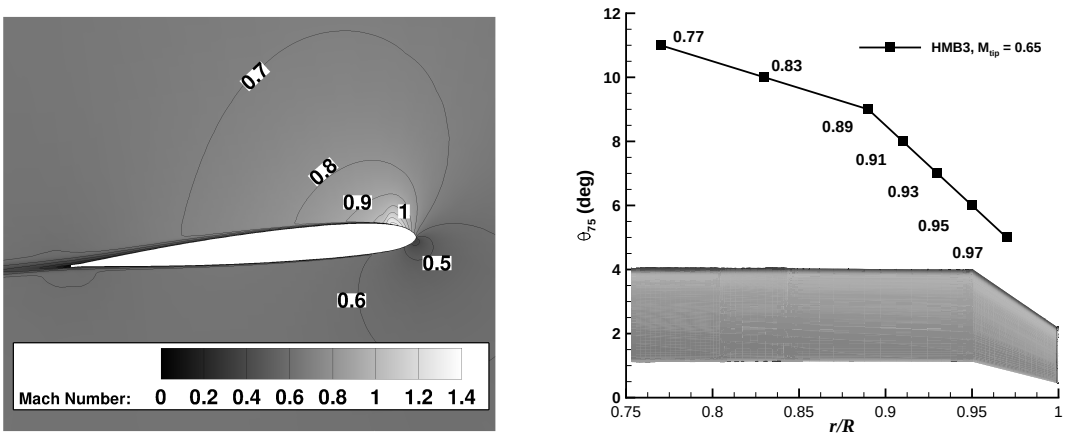

(a) (b)

Fig. 9: Contours of Mach number on a plane extracted at r/R = 0.975 (left) and radial location where the local flow becomes first supersonic as function of θ_{75} (right).

models are based on flow visualisation studies of the rotor wake flow, which is related to the geometric rotor parameters like the number of blades, aspect ratio, chord, solidity, thrust coefficient, and linear twist angle. The prediction of the trajectory, which is captured up to 3-blade passages (wake age of $270°$ for a four-bladed rotor) is in good agreement with both empirical models. The effect of the collective pitch angle (θ_{75} = $5.0°$, $7.0°$, and $9.0°$) on the trajectory of the tip vortex is also investigated and it is depicted in Figure 10 (b). Until the first passage (wake age of $90°$), a slow convection of the tip vortices is seen in vertical displacement (-z/R). As result of the passage of the following blade, a linear increment of the vertical displacement of the wake is found, mainly due to the change in the downwash velocity. As the thrust coefficient is increased, a more rapid vertical displacement is seen for the tip vortices. On the other hand, the radial displacement is less sensitive to changes on the collective pitch angles, reaching asymptotic values approximately at r/R = 0.8.

Likewise, the vortex core size (based on vorticity magnitude) was computed at collective pitch angles of θ_{75} = $5.0°$, $7.0°$, and $9.0°$. Figure 11 presents the growth of the vortex core radius normalised by the equivalent blade chord (c_e=3.07 inches):

$$c_e = 3 \int_o^1 c(r)\, r^2\, dr. \tag{4}$$

A rapid growth of the radius of the tip vortex is seen, as function of the wake age. Up to the first passage (wake age of $90°$), a moderate effect of the collective pitch angles on the core size of the vortex wake is also observed, with cores reaching three times their initial values. Therefore, for the third passage (wake age of $270°$), the values of the core reached four times their initial value. This rapid growth it due to numerical diffusion and grid density effects.

The flowfield around the S-76 blade is visualised using iso-surfaces of Q criteria 12. The collective was set to $7.0°$ degrees. The plots reveal that the computations capture the rotor wake up to 3 and 6 blade

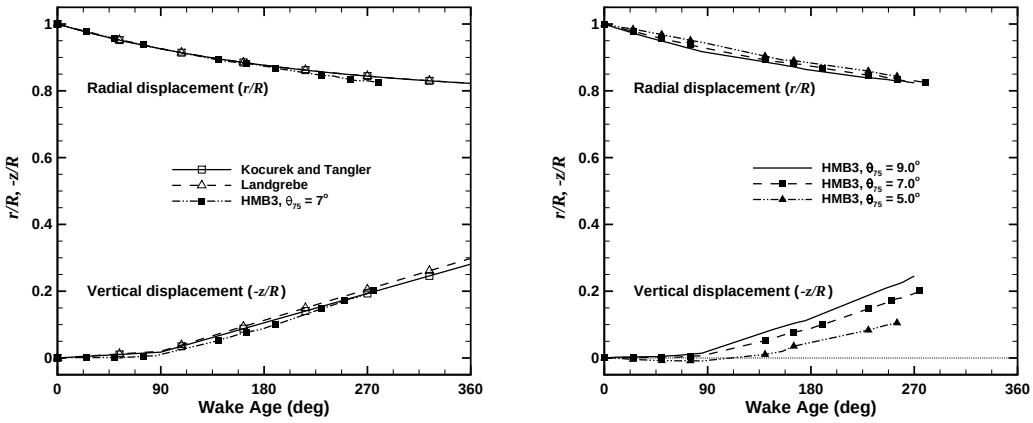

(a) (b)

Fig. 10: Comparison between the computed tip vortex displacements and the prescribed wake-models (left) and effect of the collective on the radial and vertical displacements of the tip vortices (right).

passages for the overset grids II and III, respectively. A root vortex is also seen in both computations.

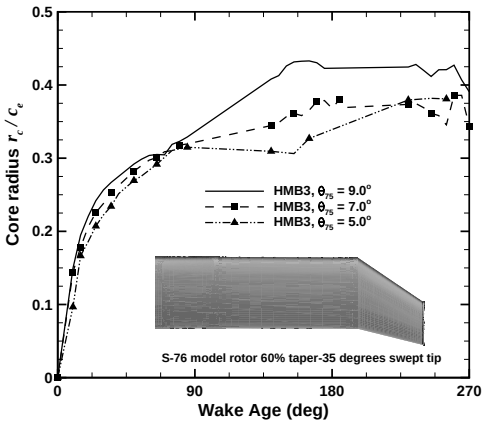

Fig. 11: Vortex core size versus wake age (in degrees) at collective pith angles of $5.0°, 7.0°$, and $9.0°$.

E. Swept-Taper Tip (Blade-Tip Mach Numbers of 0.60 and 0.55)

Hover predictions on the S-76 with 60% taper-35° swept flat tip at blade-tip Mach numbers of 0.55 and 0.60 were performed at four collective pitch angles ($6°, 7°, 8°$ and $9°$). For this section, integrated performance is evaluated using the available experimental data. The medium chimera grid was used as consequence of its good performance obtained previously at blade-tip Mach number of 0.65, and its low computational cost.

Figures 13 shows the figure of merit at blade-tip Mach numbers of 0.6 (a) and 0.55 (b), respectively, as a function of the blade loading coefficient C_T/σ. Comparisons with the momentum-based estimation of the figure of merit are also given, with induced power factor k_i of 1.1 and overall profile drag coefficient C_{D0} of 0.01. It is seen that the CFD predictions slightly over-predict the values of figure of merit at blade collective

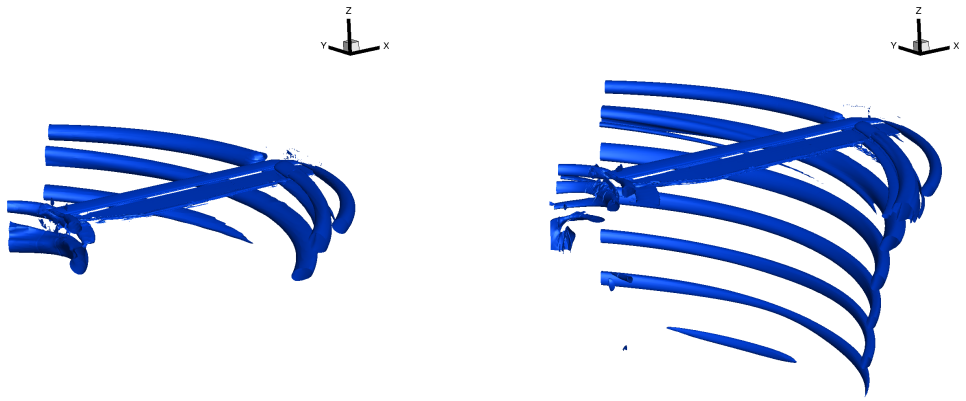

(a) (b)

Fig. 12: Wake visualisation of the S-76 model-scale in hover using the Q criterion for overset grids II (left) and III (right) of Table 2.

angles of $8°$ and $9°$. Nevertheless, the calculations show a reliable correlation to overall performance, where the tip Mach number effect is well captured.

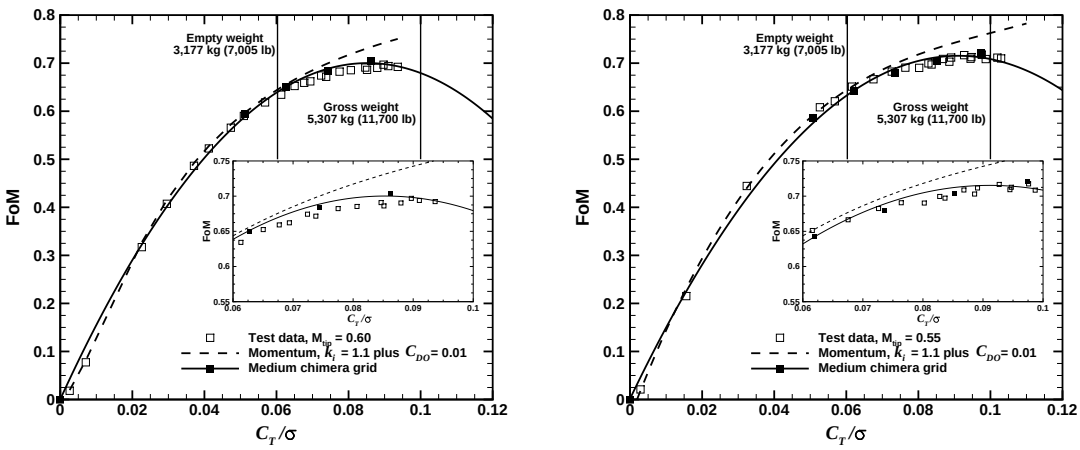

(a) $M_{\text{tip}} = 0.6$. (b) $M_{\text{tip}} = 0.55$.

Fig. 13: Figure of merit versus blade loading coefficient for the S-76 model rotor with 60% taper-$35°$ swept tip at blade-tip Mach numbers of 0.6 (left) and 0.55 (right).

F. Rectangular Tip (Blade-Tip Mach Numbers of 0.65 and 0.6)

The effect of the rectangular tip on the rotor performance of the 1/4.71 scale S-76 is evaluated here. Figures 14 (a) and (b) show the figure of merit for collective angles from $4°$ to $8°$ and $6.5°$, $7.5°$, and $8.5°$ at blade-tip Mach numbers of 0.65 and 0.60, respectively. Comparisons with the momentum-based estimation of the figure of merit are also given with induced power factor k_i of 1.15 and overall profile drag coefficient C_{D0} of 0.01. Note that rectangular tips present a higher induced power factor, leading to decrease the FoM.

At blade-tip Mach number of 0.65, it can be seen that CFD predictions over-predict the values of figure of merit at collective pitch angles of 7 and 8 degrees. However, CFD results for performance at blade-tip Mach number of 0.60 reveal good agreement with the experimental data.

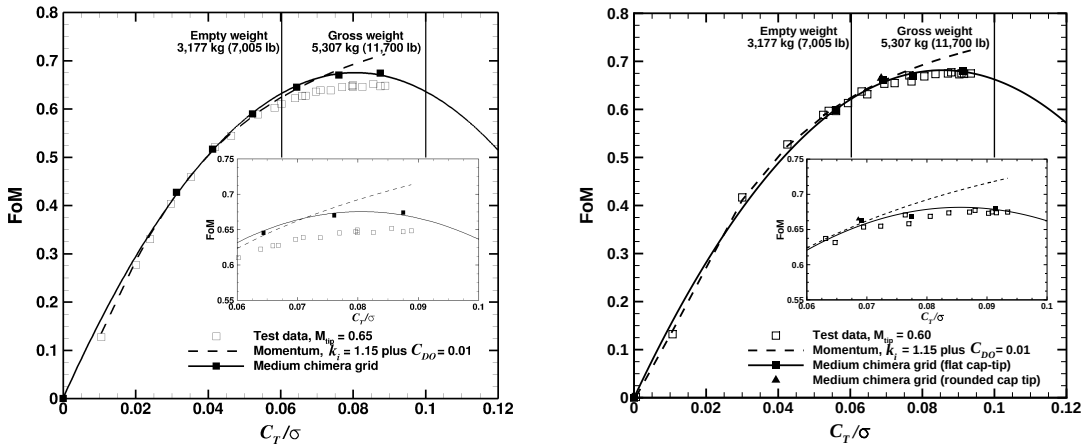

(a) $M_{\text{tip}} = 0.65$.

(b) $M_{\text{tip}} = 0.60$.

Fig. 14: Figure of merit versus blade loading coefficient for the S-76 model rotor with rectangular tip at blade-tip Mach numbers of 0.65 (left) and 0.60 (right).

For this case, the effect of using rounded tip-caps (represented with triangles in Figure 14 (b)) was also evaluated, showing a weak effect on the FoM. The CFD results were able to predict the trend of the rectangular tip and indicate that this shape is of lower performance than the swept-tapered one.

G. Anhedral Tip (Blade-Tip Mach Number of 0.65 and 0.60)

Figure of merit as function of the blade loading coefficient for the S-76 model rotor with 60% taper-35° swept-20° anhedral tip, are given in Figure 15 at blade-tip Mach numbers of 0.65 and 0.60. Rounded tip-caps were also computed at collective pitch of 7.5°. As shown for the swept-tapered tip, the effect of rounding is weak. Overall, the CFD predictions are in good agreement with the experimental data at low, medium and high thrust. The results for this tip, broadly follow the swept-tapered tip trends. The main difference is the higher figure of merit that is obtained due to the additional off-loading of the tip provided by the anhedral. This is a known effect [1] and is captured accurately by the present computations.

To assess the effect of the anhedral angle (16.234 degrees instead to 20 degrees) on the figure of merit, a comparison between both cases is shown in Figure 15 (b) at blade-tip Mach number of 0.6 and collective 9.5°. It is found that an anhedral of 16.234 degrees resulted in a figure of merit very close the value obtained for 20 degrees. A difference of 0.2 counts of FoM is computed with the 20 degrees anhedral giving ever so slightly higher FoM.

H. Effect of the Tip Shape

The effect of the tip shape on the figure of merit at blade-tip Mach number of 0.65 is depicted in Figure 16. Hover performance predictions are represented by solid lines for the rectangular tip, dashed lines are

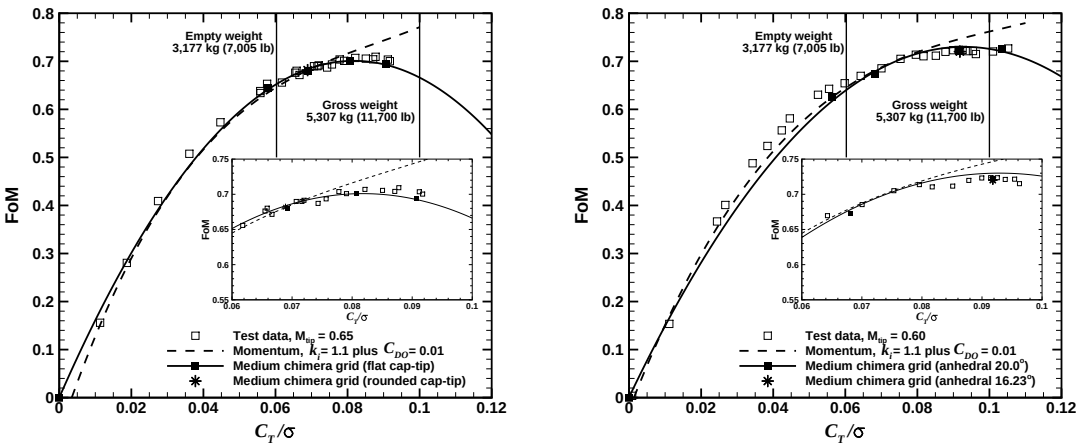

(a) $M_{\text{tip}} = 0.65$.

(b) $M_{\text{tip}} = 0.60$.

Fig. 15: Figure of merit versus blade loading coefficient for the S-76 model rotor with 60% taper-35° swept-20° anhedral tip at blade-tip Mach numbers of 0.65 (left) and 0.60 (right).

used for the swept-tapered tip, and dash-dotted lines for the swept-tapered tip with anhedral. Experimental data is also shown using open symbols. Considering the experimental data, the swept-tapered with anhedral and the rectangular tips represent the upper and lower bounds of the experimental figure of merit, while the swept-tapered tip is located within this band. This is in line with the HMB predictions that are in acceptable agreement with the experimental data across the range of blade thrusts, and tip shapes considered.

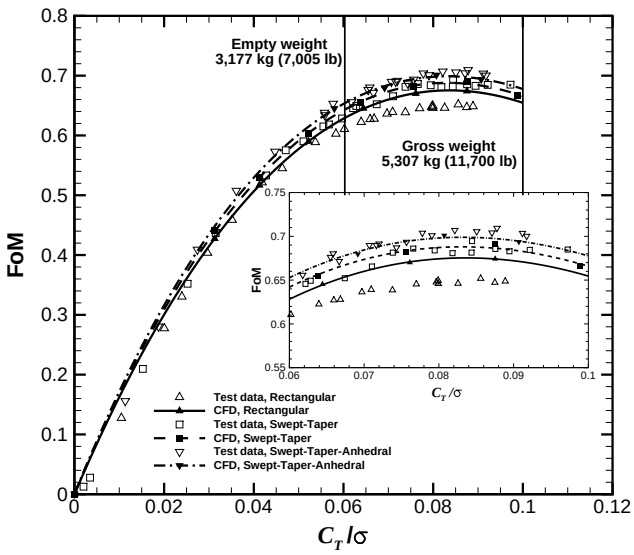

Fig. 16: Effect of the blade-tip shape on the figure of merit for the S-76 model rotor at tip Mach number of 0.65.

I. Aeroacoustic Study

The Helicopter Ffowcs Williams-Hawkings (HFWH) aeroacoustic code is used here to predict the mid and farfield noise on the 1/4.71 scale S-76 main rotor. It solves the Farassat 1A formulation (also known as retarded-time formulation) of the original Ffowcs Williams-Hawkings (FW-H) equation [46], which is mathematically represented by:

$$\begin{aligned} 4\pi a_\infty^2(\rho(\mathbf{x},\mathbf{t})-\rho_\infty) = \frac{\partial}{\partial t}\int \frac{\rho_\infty u_n}{r}\delta(f)\frac{\partial f}{\partial \mathrm{x_j}}\,\mathrm{dS(y)} - \frac{\partial}{\partial \mathrm{x_i}}\int \frac{P_{ij}}{r}\delta(f)\frac{\partial f}{\partial \mathrm{x_j}}\,\mathrm{dS(y)} \\ + \frac{\partial^2}{\partial \mathrm{x_i x_j}}\int \frac{T_{ij}(\mathbf{y},\mathbf{t}-\mathbf{r}/\mathbf{c})}{r}\,\mathrm{dV(y)}. \end{aligned} \tag{5}$$

where $T_{ij} = \rho u_i u_j + P_{ij} - c^2(\rho-\rho_\infty)\delta_{ij}$ is known as the Lighthill stress tensor [47], which may be regarded as an "acoustic stress". The first and second terms on the right-hand of Eq. 5 are integrated over the surface f, whilst the third term is integrated over the volume V in a reference frame moving with the body surface. The first term on the right-hand, represents the noise that is caused by the displacement of fluid as the body passes, which known as thickness noise. The second term accounts for noise resulting from the unsteady motion of the pressure and viscous stresses on the body surface, which is the main source of loading, blade-vortex-interaction, and broadband noise [48]. If the flowfield is not transonic or supersonic, these two source terms are sufficient [48]. The fluctuation of pressure is computed by integrating the Ffowcs Williams-Hawkings equation on an integration surface placed away from the solid surface. The time-dependent pressure signal that appears in Eq. 5 is obtained by transforming the flow solution from the blade reference frame to the inertial reference frame.

A comparison of the noise levels radiated by the different tips at the rotor disk plane of the scale S-76 main rotor blades was carried out. A trimmed state was required for each tip, and a medium thrust coefficient C_T/σ = 0.06 and blade-tip Mach number of 0.65 were selected as a flight conditions. Table 6 reports the blade collective angle θ_{75}, coning angle β, blade loading coefficient C_T/σ, torque coefficient normalised by the rotor solidity C_Q/σ, and FoM for each shape tip at the trimmed condition. The higher figure of merit obtained by the anhedral (1.24% and 2.83% higher than the swept-taper and rectangular tips) is due to the additional off-loading of this tip. This is a known effect reported by Brocklehurst and Barakos [1].

Table 6: Performance on the 1/4.71 scale S-76 rotor with rectangular, swept-taper, and anhedral shape tips for the same blade loading coefficient C_T/σ = 0.06, and blade-tip Mach number was of 0.65. The medium chimera grid was used (grid II on Table 2) for this study.

Configuration	θ_{75} ***(deg)***	β ***(deg)***	$\mathbf{C_T/\sigma}$	$\mathbf{C_Q/\sigma}$	**FoM**	**ΔFoM [%]**
Rectangular tip	6.600	1.966	0.0600	0.00440	0.627	-
Swept-Taper tip	6.621	1.985	0.0598	0.00431	0.637	1.594
Anhedral tip	6.675	2.032	0.0600	0.00427	0.645	2.870

Due to the lack of experimental acoustic data for the S-76 in hover, a comparison with the theory was conducted in terms of thickness and loading noise predictions. Both analytical solutions are based on the

work of Gopalan [49, 50], and have been successfully employed in the helicopter community [51].

Comparisons of the theoretical and numerical thickness, loading, and total noise at the rotor disk plane are shown in Figure 17, as function of the observer distance r_H. The x-axis represents the observer time ($t = \frac{\Psi + M_{\text{tip}}(cos(\Psi)-1)}{\Omega}$), where Ψ is the local azimuth angle. As expected, the effect of the tip configuration on the numerical thickness noise is negligible. It is seen that predicted noise is in close agreement with the analytical solution, where the peak of negative-pressure are well predicted by the HFWH.

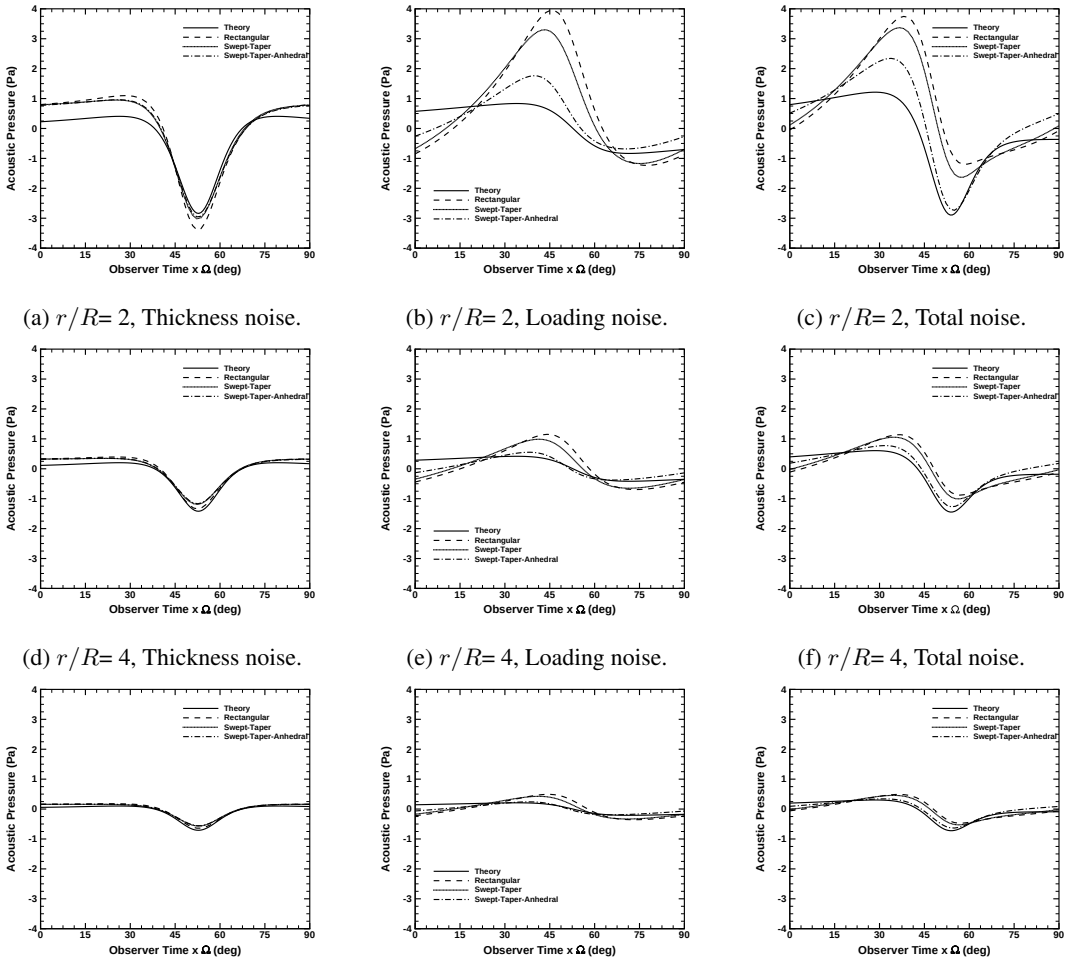

(a) r/R= 2, Thickness noise. (b) r/R= 2, Loading noise. (c) r/R= 2, Total noise.

(d) r/R= 4, Thickness noise. (e) r/R= 4, Loading noise. (f) r/R= 4, Total noise.

(g) r/R= 8, Thickness noise. (h) r/R= 8, Loading noise. (i) r/R= 8, Total noise.

Fig. 17: Comparison of theoretical and numerical thickness, loading, and total noise distributions in the rotor disk plane for the 1/4.71 scale S-76 rotor with rectangular, swept-taper, and anhedral tip configurations.

Figure 18 (a) shows the total noise as a function of the radial distance in the rotor disk plane for each tip configuration. For a radial distance r/R = 10, it is found that the swept-tapered tip is slightly louder than the anhedral with a difference of 1.83 *dB*. There are other regions, however, where this difference may be more significant. In this regards, a set of microphones were located 45° downward to the rotor disk plane, and their level of noise is reported in Table 7. A reduction of the total noise by 4.53 *dB* is gained if the anhedral

tip configuration is used. Figure 18 (b) shows the total noise as a function of the radial distance for those microphones. It is seen than the swept-tapered tip is louder than the anhedral tip. It is mainly due to the effect of the loading noise distribution, which is the main mechanism of noise generation in this direction.

Table 7: Thickness, loading, and total noise for a microphone located $45°$ downward to the rotor disk plane (r/R = 3) for the S-76 rotor blade with rectangular, swept-tapered, and anhedral tip configurations.

Configuration	**Thickness, *dB***	**Loading, *dB***	**Total, *dB***	**ΔTotal [%]**
Rectangular tip	74.09	112.42	112.43	-
Swept-Taper tip	73.93	112.27	112.28	0.13
Anhedral tip	74.26	107.88	107.91	4.02

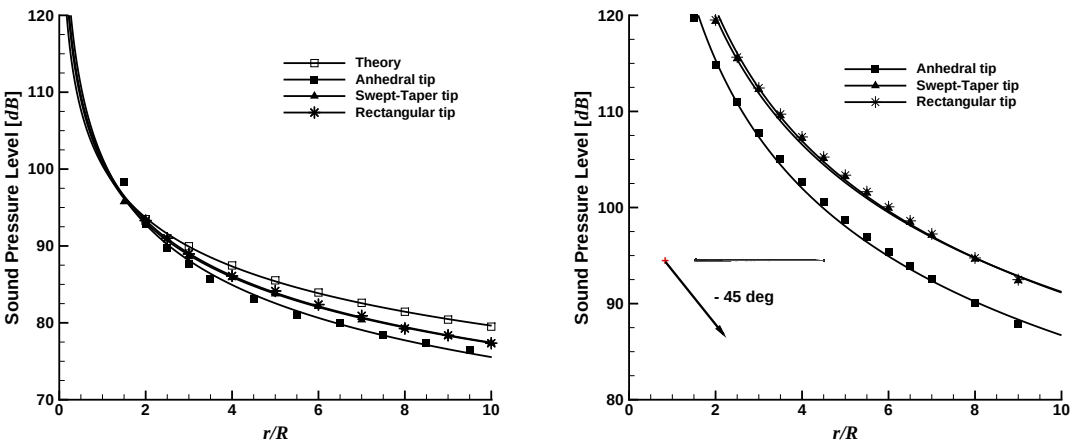

(a) (b)

Fig. 18: Total noise for the 1/4.71 scale S-76 rotor blade with rectangular, swept-taper, and anhedral tip configurations, as function of the radial distance in the rotor disk plane (left) and total noise as a function of the radial distance for a set of microphones located $45°$ downward to the rotor disk plane (right).

IV. Full-Scale S-76 Rotor Blade

The full-scale S-76 rotor was tested by Johnson [52] in the Ames 40- by 80- Foot wind tunnel for a wide range of advance ratio from 0.075 to 0.40 and an advancing side tip Mach number M_{at} range from 0.640 up to 0.965. Like the model-scale, it was found that the swept tapered tip had the better performance in forward flight mainly due to a lower power required. A further discussion of the rotor performance was reported by Stroub [53], whereas blade vibratory loads and noise were investigated by Jepson [54]. Comparison of the performance of the full-scale with the 1/5 model-scale and theoretical calculations were conducted by Balch [55]. The majority of the previous experimental tests on the full-scale S-76 did not perform hover cases. To fill this gap, a major study to establish a database on the S-76 full-scale in hover was undertaken by Shinoda [56, 57]. The NASA Ames 80- by 120- Foot Wind Tunnel was used as a hovering facility, where the S-76 rotor blade with 60% taper-$35°$ swept tip at blade-tip Mach number of 0.604 was selected.

A. Aeroelastic Analysis of the S-76 Rotor

For this study, the use of a static analysis on the S-76 full-scale rotor blade with 60% taper-35° swept tip was put forward as a means to quantify its effect on the rotor performance.

1. *Structural Model*

A structural model of the S-76 model was generated using the available data from Johnson [52] and Jepson [54]. In Figure 19 the blade is modelled using 17 elements of the CBEAM type of NASTRAN. Likewise, the rigid bar elements (RBAR) are also shown, which have no structural properties, and used to link the chord nodes to the leading edge with the trailing edge. The distributions along the radius of the Young's Modulus, Poisson's ratio, and torsional stiffness were not available, and the material properties of the UH-60A [58] were used instead. The structural properties of the blade are presented in Figure 20 which suggests that the blade suffers a reduction of the beamwise, chordwise, and torsional stiffness from the normalised radial position r/R=0.75 to the tip, corresponding to, 78.9%, 71.0%, and 86.4%, respectively. Table 8 shows a comparison of the eigenfrequency obtained using NASTRAN with DYMORE IV, and RCAS results by Monico [59] for the first three modes at the nominal speed of the rotor Ω=296 *rpm*, which suggests fair agreement.

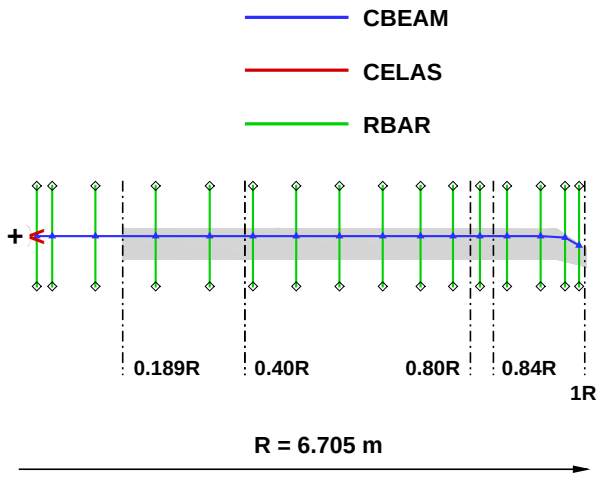

Fig. 19: Structural model of the full-scale S-76 rotor blade, showing the distribution of the 17 elements of the CBEAM type through the spanwise of the blade.

2. *Analysis of Elastic Blade Results*

Numerical simulations of the full-scale S-76 with a set of rigid and elastic rotor blades were performed at blade-tip Mach number of 0.605. For this hovering case, the blade-tip Reynolds number was set to $5.27 \cdot 10^6$,

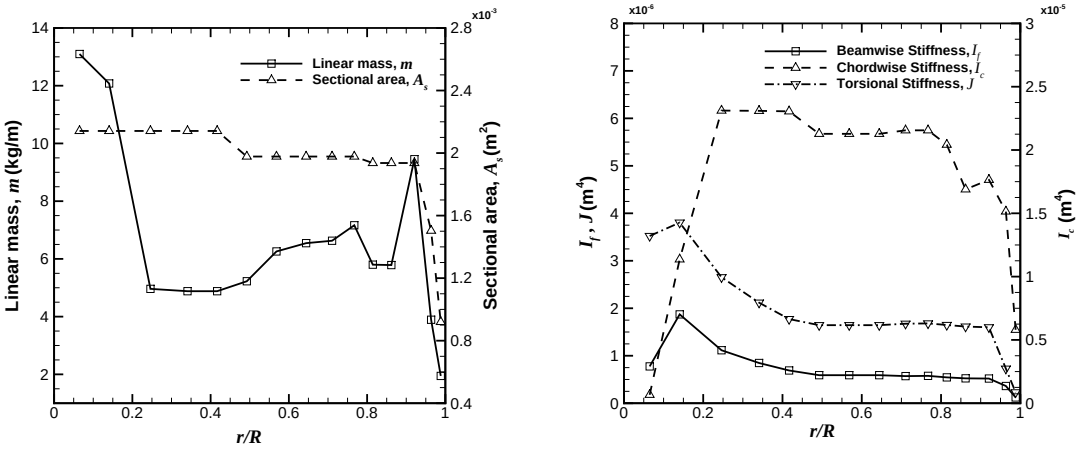

(a) (b)

Fig. 20: Sectional area and linear mass distribution (left) and chordwise, flapwise, and torsional area moments of inertia (right) for the S-76 rotor blade with 60% taper-35° swept tip [57].

Table 8: Eigenfrequencies of the full-scale S-76 rotor blade at nominal speed Ω=296 *rpm*, using NASTRAN. Comparison with the DYMORE IV and RCAS codes [59] is also shown.

Code	First mode, *Hz*	Second mode, *Hz*	Third mode, *Hz*
NASTRAN	1.22	5.03	14.80
DYMORE IV	1.52	5.07	13.22
RCAS	1.19	4.88	14.03

being 4.71 times larger than the model-scale. The importance of Reynolds number is well established in fixed wing aerodynamics. By contrast, in the case of rotary wing aerodynamics, its influence is still not well understood [60]. Moreover, the low Reynolds number of the model-scale may cause premature separation which does not occur at full-scale as a result of the turbulent boundary layer. This effect leads to increased figure of merit for the full-scale rotor.

A set of collective pitch angles corresponding to low, medium, and high thrust coefficient were simulated. It is interesting to note that coning angles were set according to Shinoda's report [57], with coincident flapping and lead-lag hinges located at $0.056R$ for the model rotor. Figure 21 (a) presents the figure of merit as a function of the blade loading coefficient C_T/σ at different collective pitch angles computed with HMB. Comparison with the experimental data of Shinoda and the Sikorsky Whirl Tower [57] is also shown. The scatter of the Shinoda data is remarkably large and two lines were best-fitted corresponding to lower and upper bounds of the test data. At low and medium thrust coefficients, the prediction of the FoM between the Sikorsky Whirl Tower and CFD with rigid blade is well captured. However, at high thrust the FoM is slightly over-predicted. On the other hand, the FoM is over-predicted if compared with the experimental data of Shinoda. The reason for this disagreement may be partly due to the variations in experimental data between the Sikorsky Whirl Tower and wind tunnels. The reason can be due to wake reingestion as a con-

sequence perhaps of mild in-ground effect and tunnel walls. Considering the aeroelastic curve (lines with stars), it is found that at low and medium thrust coefficients C_T/σ = 0.031 and 0.057, the FoM does not suffer a significant change. In contrast, a better agreement between CFD and experimental data at high thrust is found. In fact, the drop in performance (3.48% of FoM at C_T/σ = 0.087) is a consequence of the lower twist introduced by the structural properties of the blade.

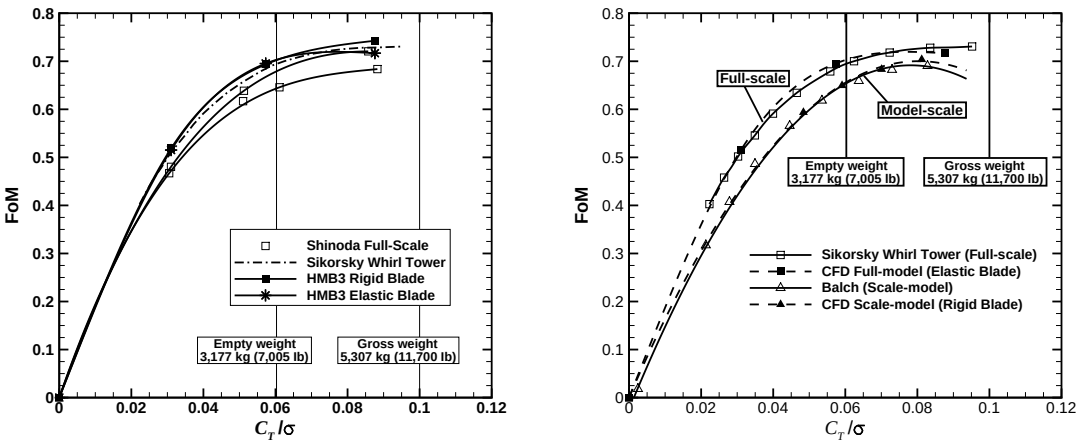

(a) Effect of the rigid/elastic blades.

(b) Effect of the Reynolds number.

Fig. 21: Effect of the rigid/elastic blades (left) and Reynolds number (b) on the figure of merit for the S-76 rotor blade with 60% taper-35° swept tip.

B. Comparison between Full and Model-Scale Rotors

This section presents a comparison between the full and model-scale S-76 rotors in terms of figure of merit. When comparing model-scale to full-scale rotor performance data, some considerations should first be made. First, the full-scale blade-tip Mach number must be matched. Thus, the rotational velocity of the model-scale rotor would be multiplied by a geometric scale factor (4.71 for the S-76 rotor). Second, the Reynolds number is not possible to match if the full-scale blade-tip Mach number is kept constant for both rotors. This parameter is the main cause of differences between full-scale and model-scale rotor test data. Finally, the rotor blade elasticity should also be considered at high thrust to fully model the blade structural aeroelasticity effects.

Figure 21 (b) shows the effect of the Reynolds number on the FoM for the S-76 rotor blade with 60% taper-35° swept tip. Experimental data correspond to the Sikorsky Whirl Tower [57] for the full-scale rotor (lines with opened squares), and Balch and Lombardi [5] for the model-scale rotor (lines with opened triangles), where the blade-tip Mach number was set to 0.60. CFD results are represented by filled squares and filles triangles with dashed lines for the full-scale (elastic blades are considered) and model-scale, respectively. Analysing the experimental data, a higher FoM is observed for the full-scale rotor over the whole range of thrust coefficient. For instance, the FoM is 6.26% higher for a medium thrust coefficient (C_T/σ = 0.060) and 9.66% higher for a high thrust coefficient (C_T/σ = 0.092). This is consistent with experience,

and justified by the decrease of the aerofoil drag coefficient for increasing Reynolds number. This is also shown for the aerofoils of the S-76 rotor blade by Yamauchi [61, p. 30]. This behaviour is also observed in the CFD results, which confirms that the present method is able to capture the Reynolds number effects.

V. XV-15 Tiltrotor Blade

A. XV-15 Rotor Geometry

The three-bladed XV-15 rotor geometry was generated based on the full-scale wind tunnel model tested by Betzina in the NASA Ames 80- by 120-foot wind tunnel facility [12]. NACA 6-series five-digit aerofoil sections comprise the rotor blade, and its identity and radial location along the rotor blade is reported in Table 9.

Table 9: Radial location of the XV-15 rotor blade aerofoils [9].

$\mathbf{r/R}$	**Aerofoil**
0.09	NACA 64-935
0.17	NACA 64-528
0.51	NACA 64-118
0.80	NACA 64-(1.5)12
1.00	NACA 64-208

The main geometric characteristics of the XV-15 rotor blades [12] are summarised in Table 10. It is interesting to note that unlike convectional helicopter blades, tiltrotor blades are characterised by high twist and solidity, along with a small rotor radius.

Table 10: Geometric properties of the full-scale XV-15 rotor [12].

Parameter	**Value**
Number of blades, N_b	3
Rotor radius, R	150 inches
Reference blade chord, c_{ref}	14 inches
Aspect ratio, R/c_{ref}	10.71
Rotor solidity, σ	0.089
Linear twist angle, Θ	-40.25°

A detailed sketch of the XV-15 blade planform and the blade radial twist, and chord distributions is shown in Figure 22. The rotor blade chord is held constant, and extends at almost 80% of the rotor blade. The blade root, however, was not modelled due to the lack of information on the cuff geometry in the literature.

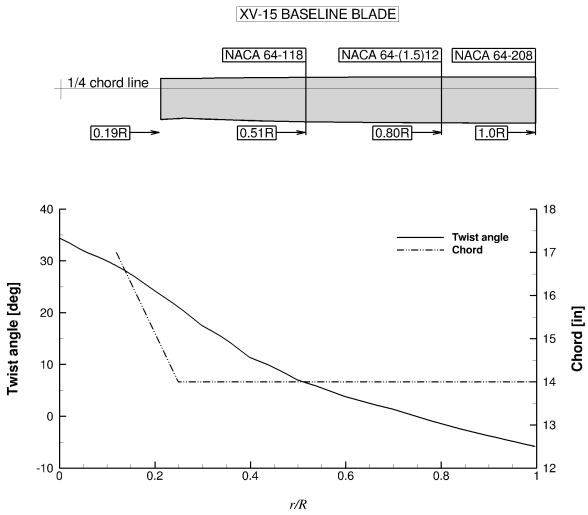

Fig. 22: Planform of the XV-15 rotor blade (above) and twist and chord distributions [62] (below).

B. XV-15 Rotor Mesh

A mesh generated using the chimera technique was used for the aerodynamic study of the XV-15 rotor. It includes a cylindrical off-body mesh used as background, and a body-fitted mesh for the blade. The use of an overset grid method allowed for the blade pitch angle to be changed by rotating the body-fitted mesh. Because the XV-15 rotor was numerically evaluated in hover and propeller modes (axial flight), only a third of the computational domain was meshed, assuming periodic conditions for the flowfield in the azimuthal direction (not applicable to stall condition). A view of the computational domain, along with the boundary conditions employed is given in Figure 23 (a). Farfield boundaries were extended to $2R$ (above rotor) and $4R$ (below rotor and in the radial direction) from the rotor plane, which assures an independent solution with the boundary conditions employed. Furthermore, an ideal rotor hub was modelled and approximated as a cylinder, extending from inflow to outflow with a radius of $0.05R$.

A C-topology was selected for the leading edge of the blade, while an H-topology was employed at the trailing edge. This configuration permits an optimal resolution of the boundary layer due to the orthogonality of the cells around the surface blade (Figure 23 (b)). The height of the first mesh layer above the blade surface was set to $1.0 \cdot 10^{-5} c_{\text{ref}}$, which leads to y^+ less than 1.0 all over the blade. Considering the chordwise and spanwise directions of the blade, 264 and 132 mesh points were used, while the blunt trailing-edge was modelled with 42 mesh points.

To guarantee a mesh independent solution, two computational domains were built. Table 11 lists the grids used and shows the breakdown of cells per blade. The coarse and medium meshes have 6.2 and 9.6 million cells per blade (equivalent to 18.6 and 28.8 million cells for three blades), with the same grid resolution for the body-fitted mesh (3.6 million cells). The background mesh, however, was refined at the wake and near-body regions, increasing the grid size from 2.6 to 6 million cells.

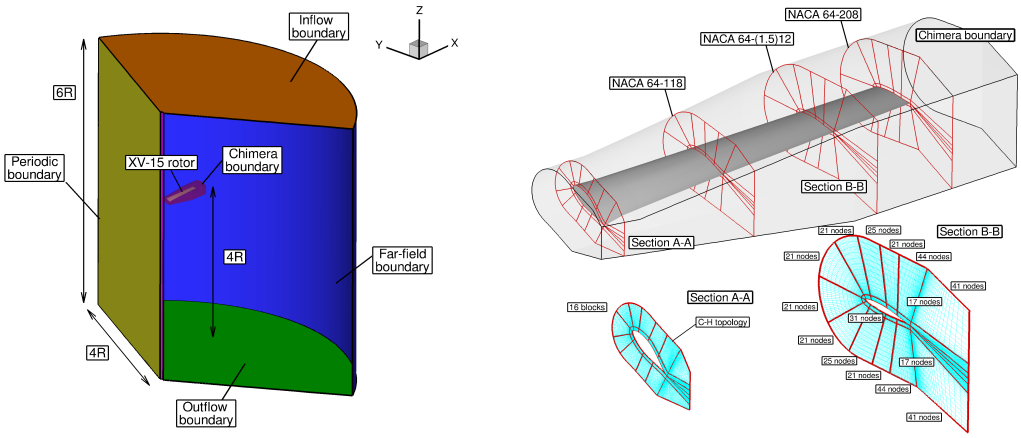

(a) Computational domain.

(b) XV-15 rotor mesh.

Fig. 23: Computational domain and boundary conditions employed (left) and detailed view of the XV-15 rotor mesh (right).

Table 11: Meshing parameters for the XV-15 rotor mesh.

	Coarse Mesh	**Medium Mesh**
Background mesh size (cells)	2.6 million	6.0 million
Blade mesh size (cells)	3.6 million	3.6 million
Overall mesh size (cells)	6.2 million	9.6 million
Height of the first mesh layer at blade surface	$1.0 \cdot 10^{-5} c_{\text{ref}}$	$1.0 \cdot 10^{-5} c_{\text{ref}}$

C. Test Conditions

Table 12 summarises the conditions employed and computations performed in hover and propeller modes. For the hover mode, the tip Mach number was set to 0.69, and four blade collective angles were considered, corresponding to low, medium, and high disc loadings. The Reynolds number, based on the reference blade chord of 14 inches and on the tip speed, was $4.95 \cdot 10^6$. The cruise condition was modelled at 0 ft (ISA+0°), with a tip Mach number of 0.54 and advance ratio 0.337. The Reynolds number for this case was $4.50 \cdot 10^6$, again based on the reference blade chord and rotor tip speed (with no account for the advance velocity).

Table 12: Flow conditions for the full-scale XV-15 tiltrotor blade.

	Helicopter Mode	**Aeroplane Mode**
Blade-tip Mach number (M_{tip})	0.69	0.54
Reynolds number (Re)	$4.95 \cdot 10^6$	$4.50 \cdot 10^6$
Blade pitch angle (θ_{75})	$3°, 5°, 10°, 13°$	$26°, 27°, 28°, 28.8°$
Grid	Coarse and Medium	Coarse and Medium
Turbulence model	k-ω SST	k-ω SST

All flow solutions were computed by solving the RANS equations, coupled with Menter's k-ω SST turbulence model [39]. The flow equations were integrated with the implicit dual-time stepping method of HMB, using a pseudo-time Courant–Friedrichs–Lewy (CFL) equal to 4 for the helicopter mode computations, and equal to 2 for the aeroplane mode. Typically, 40,000 iterations were necessary to drop the residual by 6 orders of magnitude for the flow solutions.

Solutions were computed on 232 cores of the high performance computer cluster of Glasgow University, comprised of Intel Xeon E5620 processors. For the S-76 case with the medium chimera grid (7.5 million cells per blade), the wall-clock time was 24.8 hours, whereas the XV-15 rotor blade with the coarse mesh (6.2 million cells per blade) needed 17.1 hours to achieve a fully converged solution.

D. Helicopter Mode

The effect of the mesh density on the figure of merit, and torque coefficient C_Q as functions of the thrust coefficient C_T are shown in Figure 24. Experimental data of the full-scale XV-15 rotor is also shown, carried out by Felker *et al.*[9] at OARF, and Light [11] and Betzina [12] at the NASA 80×120ft wind tunnel. The majority of works on performance analysis of rotor blades do not model the hub and root apparatus, mainly due to the complexity of mesh generation. In this regard, experiments were corrected for hub and apparatus tares. Vertical lines labelled as empty (4,574 kg) and maximum gross (6,000 kg) weight, define the hovering range of the XV-15 helicopter rotor [63]. Momentum-based estimates of the figure of merit are also included, and its expression is given in Equation 6, where an induced power factor k_i of 1.1 and overall profile drag coefficient C_{DO} of 0.01 were used.

$$\text{FoM} = \frac{{C_T}^{3/2}}{\sqrt{2}\left(\sigma\frac{C_{D0}}{8} + k_i\frac{{C_T}^{3/2}}{\sqrt{2}}\right)}. \tag{6}$$

Using the obtained CFD results, a polynomial fit was computed and shown with solid lines and squares (coarse grid) or triangles (medium grid). Considering the sets of experiments, good agreement was found between them, with a maximum discrepancy of 4.11% in the figure of merit. The reason for this disagreement (4 counts of FoM) may be partly due to the variations in experimental data between wind tunnel facilities. CFD results present an excellent agreement with the test data of Betzina[12] for all blade collective angles. It is found that the effect of the grid size on the overall performance is negligible at low thrust, with a small influence at high thrust.

The comparison of the predicted and measured [9, 11, 12] peak figure of merit is reported in Table 13. Experiments performed by Felker show a higher Figure of Merit (2 counts) if compared with the Light and Betzina experiments. A large recirculation zone was reported in the 80×120 test section of NASA by Felker, which may be the reason of this disagreement. Predictions with the medium grid indicate good correlation with the experiments (0.91% respect to Betzina and Light, and 2.53% respect to Felker). These results show that the present method is able to capture the overall performance of tiltrotors. To assess if all the flow physics is accurately modelled, more detailed experimental data is needed (flow visualisations, surface pressure and

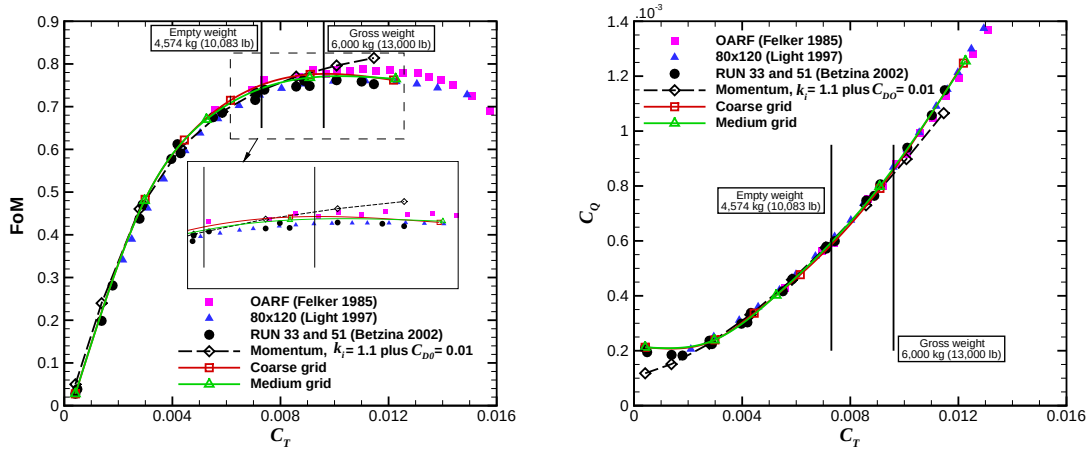

(a) FoM - C_T.

(b) C_Q - C_T.

Fig. 24: Effect of the mesh density on the figure of merit (left) and torque coefficient (right) for the full-scale XV-15 rotor.

skin friction, etc.)

Table 13: Predicted and experimental peak FoM for the full-scale XV-15 rotor.

	Experiments			**CFD**	
	Felker [9]	**Light [11]**	**Betzina [12]**	**Coarse grid**	**Medium grid**
FoM	0.788	0.761	0.761	0.776	0.768

From a point of view of the turbulence model employed, it seems that the fully turbulent flow assumption is able to capture the trend of FoM and torque coefficient (Figure 24 (b)). Similar conclusions were drawn in previous work by Kaul *et al.*[23], Yoon *et al.*[26], and Sheng *et al.*[27], where fully turbulent flows were successfully employed. Comparison between predicted and measured [13] FoM at a collective pitch angle of $10°$ is reported in Table 14. Prediction with the medium grid indicates good correlation with the experiments (0.8 counts of FoM), which highlights the ability of this medium grid in accurately predicting the FoM with a modest CPU time.

Table 14: Predicted and experimental [13] figure of merit at collective pitch angle of $10°$.

Case	**FoM**	**Difference [%]**
Coarse grid	0.775	1.97%
Medium grid	0.768	1.05%
Experiment	(0.760) [26]	-

Due to the lack of experimental surface pressure measurements, a comparison between HMB and CFD data published by Kaul *et al.*[24] using the OVERFLOW2 solver is shown in Figure 25. Three radial stations were considered (r/R=0.72, 0.83, and 0.94), and the collective pitch angle was $10°$. CFD results using HMB correspond to the coarse grid (18.6 million cells for the three blades) where the k-ω SST turbulence model [39] was employed, while Kaul's results were obtained with a grid size of 35 million cells using the Spalart-Allmaras turbulence model [25]. Despite that small variation on the predicted peak C_P, a fair agreement is found for all radial stations. Regarding the radial stations $r/R = 0.72$ and $r/R = 0.83$, it is clear that the suction peak does not exceed the critical C_P^* values, while the most outboard section ($r/R = 0.94$) reaches sonic conditions.

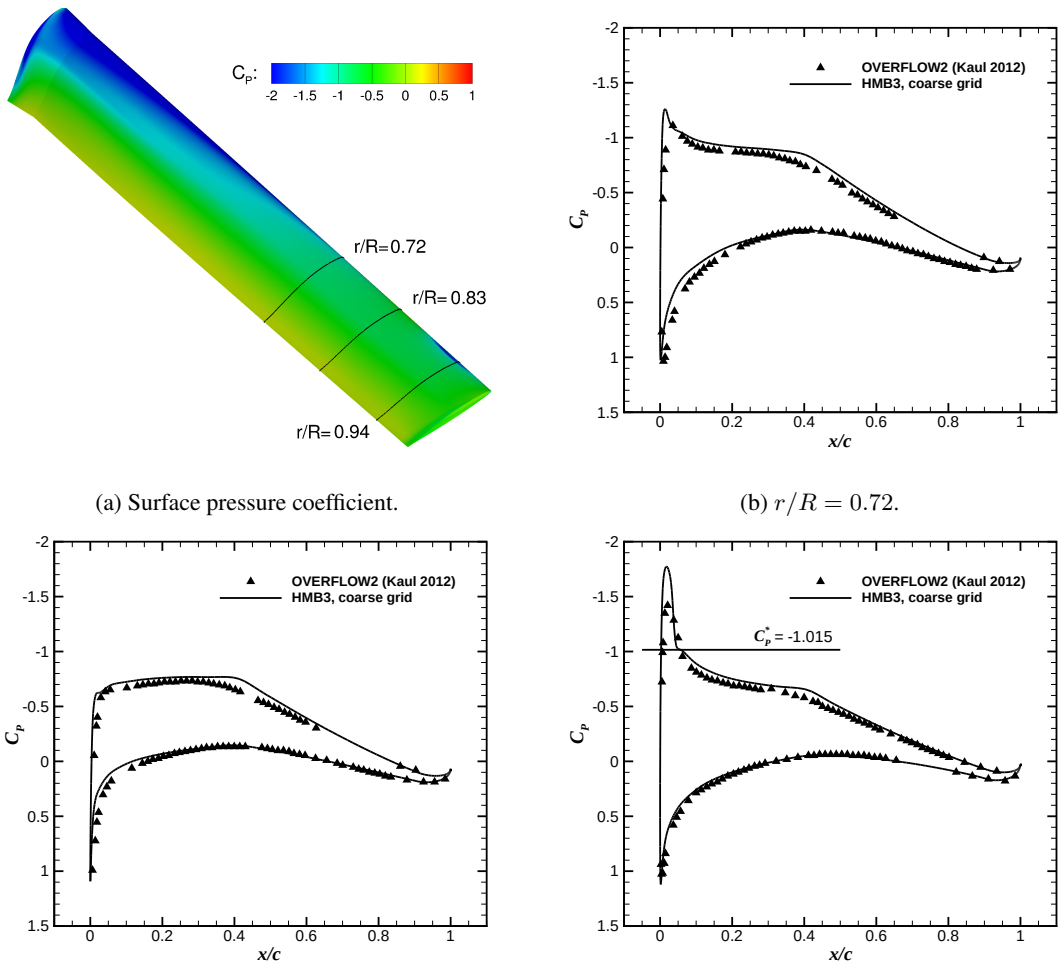

(a) Surface pressure coefficient.

(b) $r/R = 0.72$.

(c) $r/R = 0.83$.

(d) $r/R = 0.94$.

Fig. 25: Comparison of predicted surface pressure coefficient between HMB using the coarse grid and OVERFLOW2 from Kaul *et al.*[24].

E. Aeroplane Mode

Like for hover simulations, only a third of the computational domain was meshed, modelling this case as steady-state problem with periodic conditions for the flow in the azimuthal direction. Simulations were performed for medium advance ratio $\mu = 0.337$ at collective pitch angles of $26°, 27°, 28°$ and $28.8°$, and tip Mach number of 0.54 (see Table 12). In aeroplane mode, the indicator of the rotor efficiency is the propeller propulsive efficiency, which is the ratio between the useful power output of the propeller and the absorbed power:

$$\eta = \frac{C_T V_\infty}{C_Q V_{\text{tip}}}. \tag{7}$$

Figure 26 compares the total load predictions with the available experimental data [7] (represented by square symbols), where the propeller efficiency η and torque coefficient are given as function of the thrust coefficient. The experimental data reported here, were performed on a propeller test rig in the NASA 40-by-80-Foot Wind Tunnel [7], and are the only available published data for the XV-15 in aeroplane mode. HMB results with the coarse grid show an under-predicted propulsive propeller efficiency for all thrust coefficient, with a maximum discrepancy of 4.5%. However, results with the medium grid provide a good agreement with the experimental data.

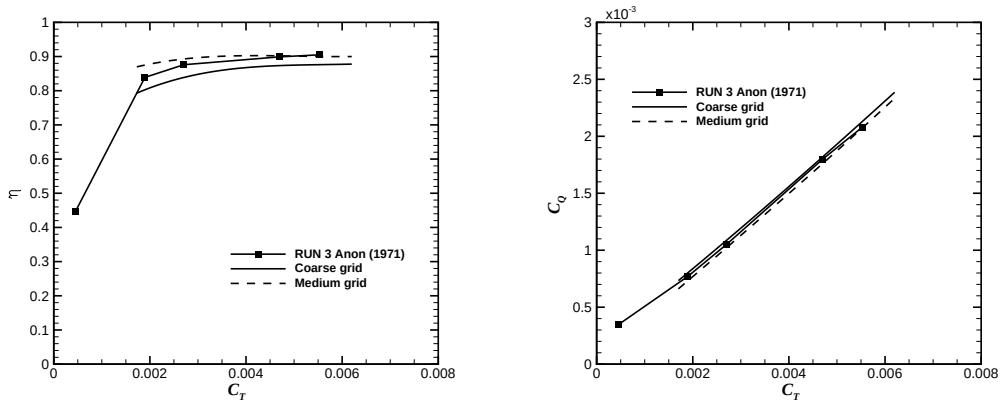

(a) Propeller propulsive efficiency - Thrust coefficient.

(b) Torque coefficient - Thrust coefficient.

Fig. 26: Propulsive propeller efficiency and torque coefficient as function of the thrust coefficient for the XV-15 rotor blade in propeller mode configuration.

F. Effect of the Turbulence Model

In this study, the effect of the $k - \omega$ SST-γ transition model is investigated in predicting the figure of merit. The predicted skin friction coefficient is compared with measurements by Wadcock *et al.*[13]. Moreover, a comparison with the solution obtained with the fully-turbulent k-ω SST model is presented. For this case, a matched grid was used, which has 10.2 million cells per blade.

Figures 27 and 28 show the computed skin friction coefficient C_f compared with the available experimental data of Wadcock *et al.*[64] for collective pitch angles of $3°$ and $10°$ at the radial stations $r/R =$

$0.28, 0.50, 0.72, 0.83$ and 0.94. At low disc loading (Figure 27), the experiment shows a natural transition for all stations at about 50% chord. It seems that the present transition model is able to capture the onset and length of the natural transition with some discrepancies found at the inboard station $r/R = 0.28$. As expected, results obtained with the fully-turbulent model indicate lack of transition. Moreover, the values of skin friction coefficient are under and over-predicted in the laminar and turbulent flow regions. Considering the C_f at collective pitch angle of $10°$ (Figure 28), the experimental C_f presents a similar pattern as seen for the lower collective pitch angles. However, the onset of the natural transition is moved towards the leading edge, with a fully-turbulent flow region observed at the outboard station $r/R = 0.94$. Results corresponding to the transition model accurately predicted the onset location and length of the transition. This physical phenomenon is not captured by the fully-turbulent solution. The surface skin friction coefficient of both turbulence models is shown in Figure 29, where the laminar-turbulent region can be only identified for the k-ω SST-γ model.

Once the distribution of skin friction coefficient was analysed, the impact of the turbulence model on the hover performance of the XV-15 blade was investigated. Table 15 reports the predicted C_T, C_Q, and FoM using the fully-turbulent $k - \omega$ SST and transition model k-ω SST-γ at two disc loading conditions. It is shown that results are mildly sensitive to the turbulence model employed, with a higher figure of merit presented by the transition model.

	$\mathbf{C_T}$	$\mathbf{C_Q}$	**FoM**
FT $3°$	0.00293	0.000249	0.450
TM $3°$	0.00297	0.000223	0.512
FT $10°$	0.00906	0.000807	0.756
TM $10°$	0.00909	0.000803	0.763

Table 15: Comparison of predicted C_T, C_Q, and FoM at $3°$ and $10°$ collective angles between the fully-turbulent $k - \omega$ SST and transition model k-ω SST-γ. Conditions employed: $M_{\text{tip}} = 0.69$ and $Re = 4.95 \cdot 10^6$. FT=Fully-Turbulent; TM=Transitional-Model.

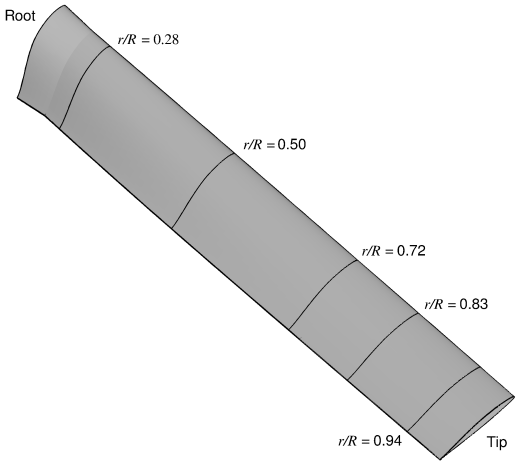

(a) Radial stations.

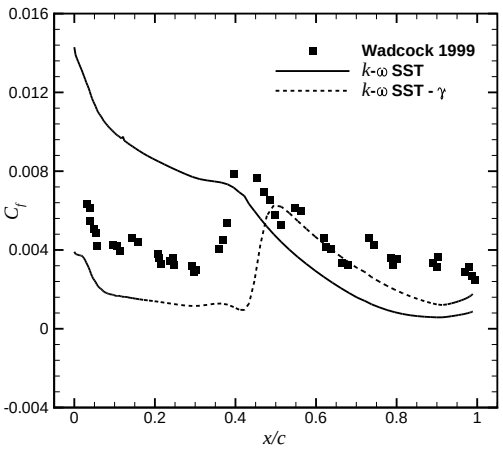

(b) $r/R = 0.28$.

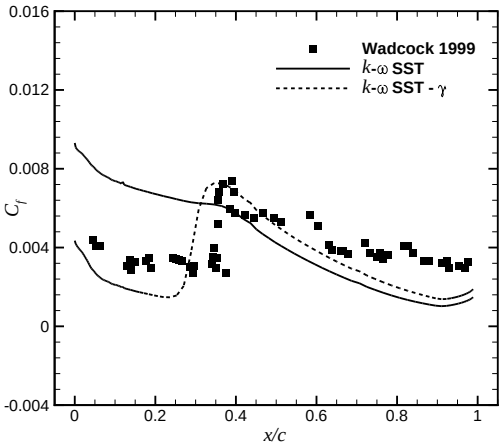

(c) $r/R = 0.50$.

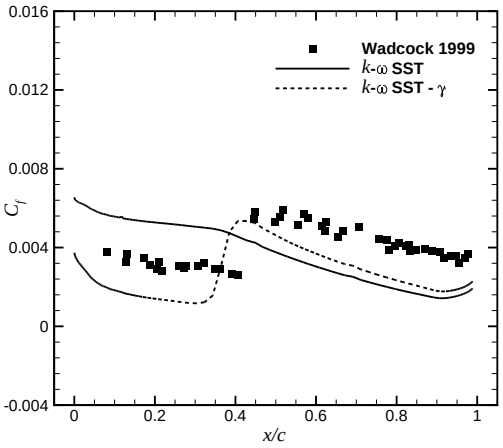

(d) $r/R = 0.72$.

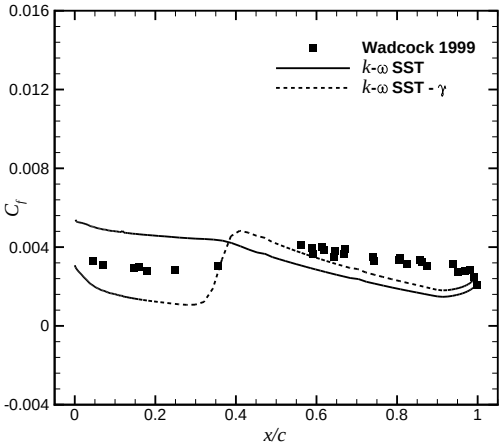

(e) $r/R = 0.83$.

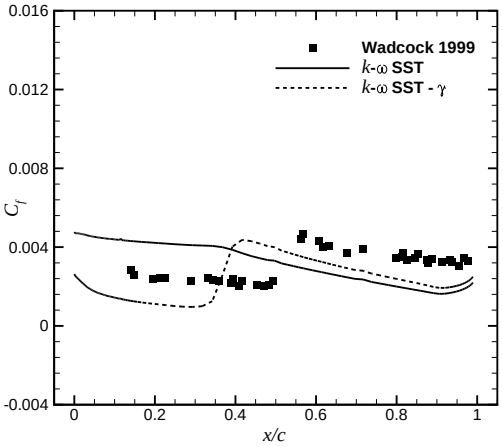

(f) $r/R = 0.94$.

Fig. 27: Comparison between the computed skin friction coefficient using a fully turbulent and transition model solutions with the experimental data of Wadcock *et al.*[64]. Conditions employed: $M_{\text{tip}} = 0.69$, $Re = 4.95 \cdot 10^6$, and $\theta_{75} = 3°$.

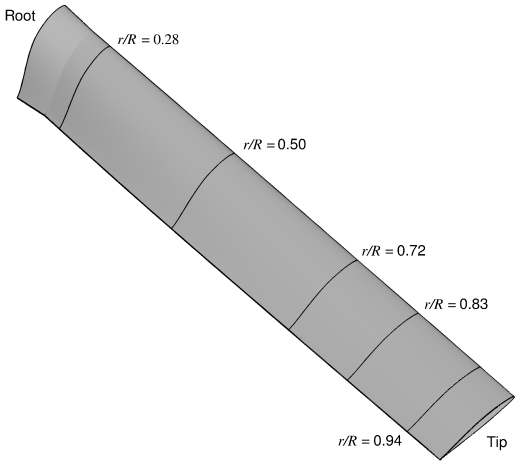

(a) Radial stations.

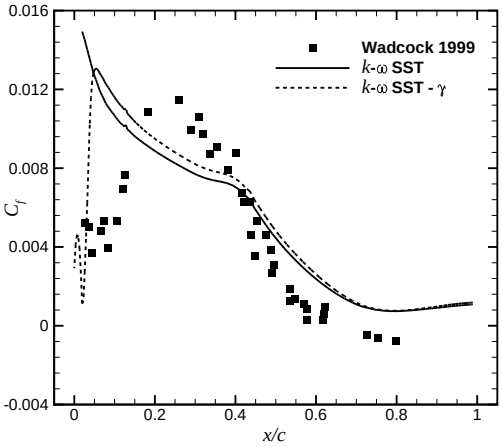

(b) $r/R = 0.28$.

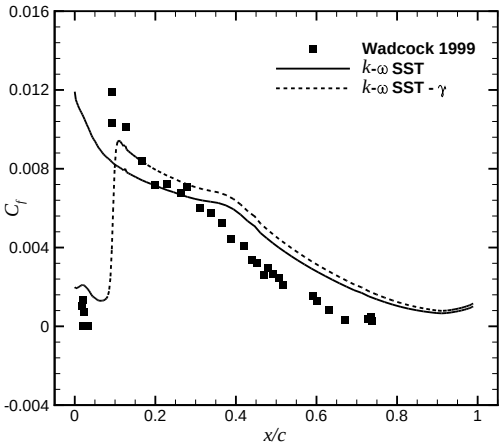

(c) $r/R = 0.50$.

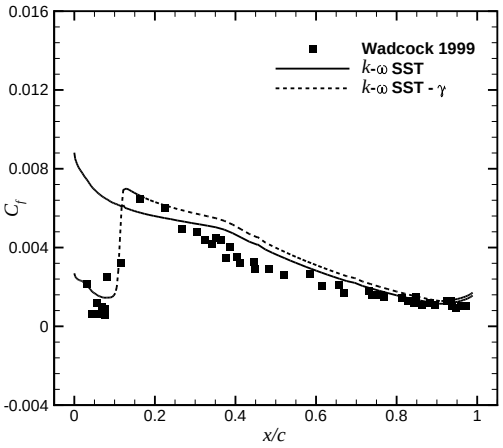

(d) $r/R = 0.72$.

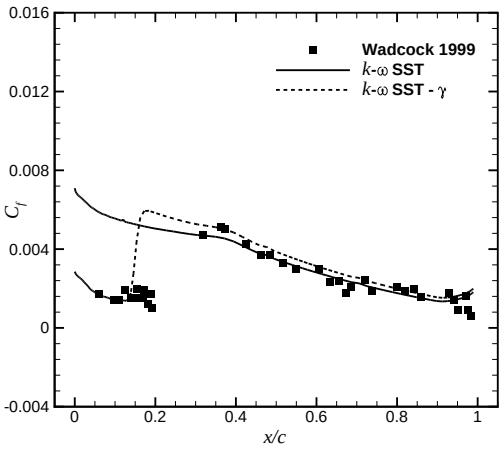

(e) $r/R = 0.83$.

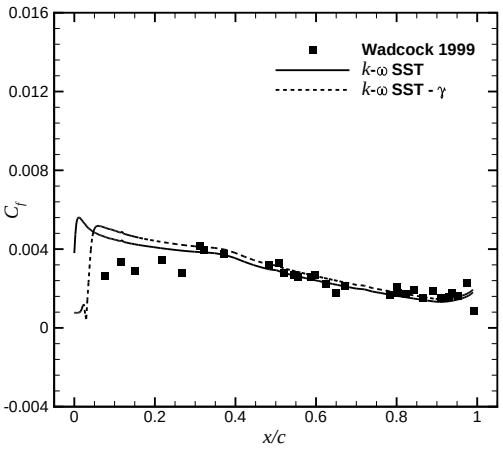

(f) $r/R = 0.94$.

Fig. 28: Comparison between the computed skin friction coefficient using a fully turbulent and transition model solutions with the experimental data of Wadcock *et al.*[64]. Conditions employed: $M_{\text{tip}} = 0.69$, $Re = 4.95 \cdot 10^6$, and $\theta_{75} = 10°$.

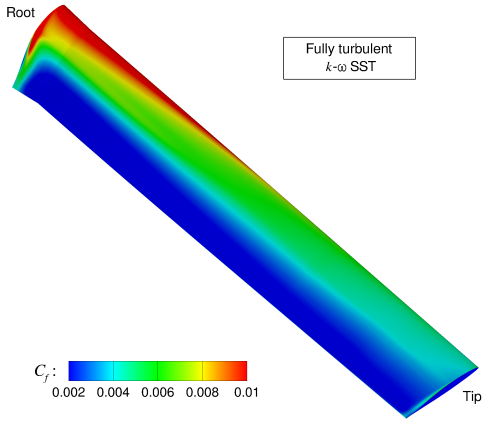

(a) Fully turbulent solution, $\theta_{75} = 3°$.

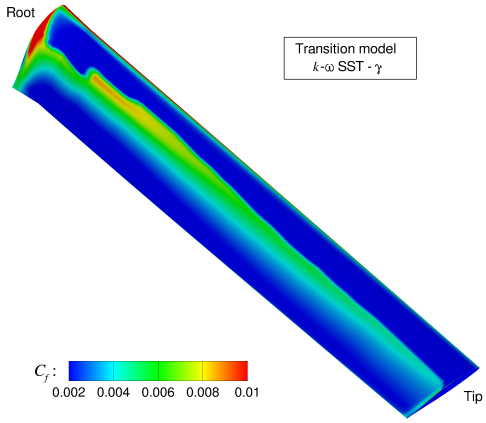

(b) Transition model solution, $\theta_{75} = 3°$.

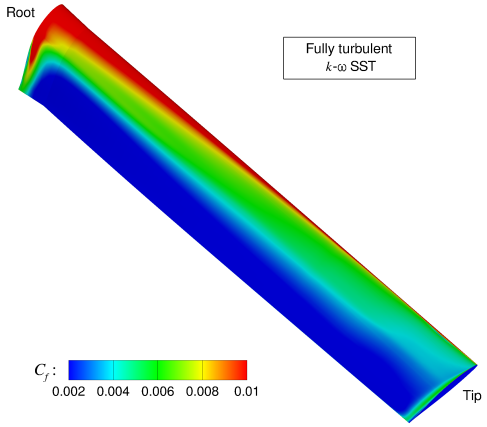

(c) Fully turbulent solution, $\theta_{75} = 10°$.

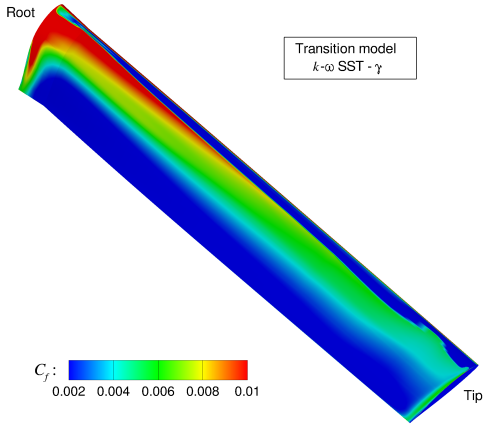

(d) Transition model solution, $\theta_{75} = 10°$.

Fig. 29: Surface skin friction coefficient for the fully turbulent and transition model cases.

VI. Conclusions

This paper demonstrates the ability of HMB solver to accurately predict the rotor hover performance at low and high disc loadings with modest computer resources. The main conclusions are:

- The effect of the tip shape and Mach number on the performance of the S-76 blade is captured by CFD with 0.1 counts of FoM for most cases, with a worst-case difference across the blade loadings and different tip shapes of 0.6 counts.
- The acoustics in hover for the S-76 blade with anhedral tip showed a reduction of the total noise by 5% if compared with the swept-taper blade.
- Aeroelastic cases showed very good agreement with whirl tower data.
- The method was able to capture the performance in the different modes for the XV-15 tiltrotor blade; hover and propeller.
- The transition onset and distribution of skin friction are well predicted and, for this case, were found to have a mild effect on the overall figure of merit.

Acknowledgements

The use of the cluster Chadwick of the University of Liverpool is gratefully acknowledged. Some results were obtained using the EPSRC funded ARCHIE-WeSt High Performance Computer (`www.archie-west.ac.uk`), EPSRC grant no. EP/K000586/1. Part of this work is funded under the HiperTilt Project of the UK Technology Strategy Board (TSB) and Leonardo Helicopters under Contract Nr. 101370.

[1] Brocklehurst, A. and Barakos, G. N., "A Review of Helicopter Rotor Blade Tip Shapes," *Progress in Aerospace Sciences*, Vol. 56, No. 1, 2013, pp. 35–74, DOI: 10.1016/j.paerosci.2012.06.003.

[2] Johnson, W., *Helicopter Theory*, Princeton University Press, New Jersey, 1980.

[3] Balch, D. T., Saccullo, A., and Sheehy, T. W., "Experimental Study of Main Rotor/Tail Rotor/Airframe Interactions in Hover - Volume I," NASA CR–166485, June 1983.

[4] Balch, D. T., "Experimental Study of Main Rotor/Tail Rotor/Airframe Interactions in Hover," *Journal of the American Helicopter Society*, Vol. 30, No. 2, 1985, pp. 49–56, DOI:http://dx.doi.org/10.4050/JAHS.30.49.

[5] Balch, D. T. and Lombardi, J., "Experimental Study of Main Rotor Tip Geometry and Tail Rotor Interactions in Hover. Vol I - Text and Figures," NASA CR–177336, Feb. 1985.

[6] Balch, D. T. and Lombardi, J., "Experimental Study of Main Rotor Tip Geometry and Tail Rotor Interactions in Hover. Vol II - Run Log and Tabulated Data Progress Report," NASA CR–177336, Feb. 1985.

[7] "Advancement of Proprotor Technology, Task II - Wind-Tunnel Test Results," NASA CR–114363, Sept. 1971.

[8] Weiberg, J. A. and Maisel, M. D., "Wind-Tunnel Tests of the XV-15 Tilt Rotor Aircraft," NASA TM–81177, April 1980.

[9] Felker, F. F., Betzina, M. D., and Signor, D. B., "Performance and Loads Data from a Hover Test of a Full-Scale XV-15 Rotor," NASA TM–86833, Sept. 1985.

[10] Bartie, K., Alexander, H., McVeigh, M., Mon, S. L., and Bishop, H., "Hover Performance Tests of Baseline Meter and Advanced Technology Blade (ATB) Rotor Systems for the XV-15 Tilt Rotor Aircraft," NASA CR–114626, Oct. 1986.

[11] Light, J. S., "Results from an XV-15 Rotor Test in the National Full-Scale Aerodynamics Complex," *Proceedings of the 53rd American Helicopter Society Annual Forum*, AHS, Virginia Beach, Virginia, 1997.

[12] Betzina, M. D., "Rotor Performance of an Isolated Full-Scale XV-15 Tiltrotor in Helicopter Mode," *Proceedings of the American Helicopter Society Aerodynamics, Acoustics, and Test and Evaluation Technical Specialist Meeting*, AHS, San Francisco, CA, 2002, pp. 1–12.

[13] Wadcock, A. J., Yamauchi, G. K., and Driver, D. M., "Skin Friction Measurements on a Hovering Full-Scale Tilt Rotor," *Journal American Helicopter Society*, Vol. 99, No. 4, 1999, pp. 312–319.

[14] Hariharan, N., Egolf, A., and Sankar, L., "Simulation of Rotor in Hover:Current State and Challenges," *Proceedings of the 52nd Aerospace Sciences Meeting*, AIAA, National Harbor, Maryland, 2014, pp. 1–28.

[15] Hariharan, N., Egolf, A., and Sankar, R. N. L., "Helicopter Rotor Aerodynamic Modeling in Hover:AIAA Standardized Hover Evaluations," *Proceedings of the 53rd Aerospace Sciences Meeting*, AIAA, Kissimmee, Florida, 2015, pp. 1–34.

[16] Sheng, C., Zhao, Q., and Wang, J., "S-76 Rotor Hover Prediction Using U2NCLE Solver," *Proceedings of the 52nd Aerospace Sciences Meeting*, AIAA, National Harbor, Maryland, 2014, pp. 1–19.

[17] Langtry, R. B., *A Correlation-Based Transition Model using Local Variables for Unstructured Parallelized CFD codes*, Ph.D. thesis, University of Stuttgart, Germany, May 2006.

[18] Langtry, R. B. and Menter, F. R., "Correlation-Based Transition Modeling for Unstructured Parallelized Computational Fluid Dynamics Codes," *AIAA Journal*, Vol. 47, No. 12, 2010, pp. 2895–2906, DOI: 10.2514/1.42362.

[19] Jain, R. K. and Potsdam, M. A., "Hover Predictions on the Sikorsky S-76 Rotor using Helios," *Proceedings of the Fifty-Second Aerospace Sciences Meeting*, AIAA, National Harbor, Maryland, 2014, pp. 1–21.

[20] Narducci, R., "OVERFLOW Simulation of Rotors in Hover: The Boeing Company," *Proceedings of the 52nd Aerospace Sciences Meeting*, AIAA, National Harbor, Maryland, 2014, pp. 1–9.

[21] Narducci, R., "Hover Performance Assessment of Several Tip Shapes using OVERFLOW," *Proceedings of the 53rd Aerospace Sciences Meeting*, AIAA, Kissimmee, Florida, 2015, pp. 1–19.

[22] Tadghighi, H., "Helios Simulation of Rotors in Hover: The Boeing Company," *Proceedings of the 52nd Aerospace Sciences Meeting*, AIAA, National Harbor, Maryland, 2014, pp. 1–9.

[23] Kaul, U. K. and Ahmad, J., "Skin Friction Predictions Over a Hovering Tilt-Rotor Blade Using OVERFLOW2," *Proceedings of the 29th Applied Aerodynamics Conference*, AIAA, Honolulu, Hawaii, 2011, pp. 1–19.

[24] Kaul, U. K., "Effect of Inflow Boundary Conditions on Hovering Tilt-Rotor Flows," *Proceedings of the 7th International Conference on Computational Fluid Dynamics*, ICCFD7, Big Island, Hawaii, 2012, pp. 1–19.

[25] Spalart, P. R. and Allmaras, S., "A One-Equation Turbulence Model for Aerodynamic Flows," *La Recherche Aérospatiale*, , No. 1, 1994, pp. 5–21.

[26] Yoon, S., Pulliam, T. H., and Chaderjian, N. M., "Simulations of XV-15 Rotor Flows in Hover Using OVERFLOW," *Proceedings of the 5th Decennial AHS Aeromechanics Specialists*, AHS, San Francisco, CA, 2014, pp. 1–11.

[27] Sheng, C. and Zhao, Q., "Investigations of XV-15 Rotor Hover Performance and Flow Field Using U2NCLE and HELIOS Codes," *Proceedings of the 54th Aerospace Sciences Meeting*, AIAA, San Diego, California, 2016, pp. 1–18.

[28] Gates, S., "Aerodynamic Analysis of Tiltrotors in Hovering and Propeller Modes Using Advanced Navier-Stokes Computations," *Proceedings of the 39th European Rotorcraft Forum*, ERF, Moscow, Russia, 2013, pp. 1–26.

[29] Barakos, G., Steijl, R., Badcock, K., and Brocklehurst, A., "Development of CFD Capability for Full Helicopter Engineering Analysis," *Proceedings of the 31st European Rotorcraft Forum*, ERF, Florence, Italy, 2005, pp. 1–15.

[30] Lawson, S. J., Steijl, R., Woodgate, M., and Barakos, G. N., "High performance computing for challenging problems in computational fluid dynamics," *Progress in Aerospace Sciences 2012*, Vol. 52, No. 1, 2012, pp. 19–29, DOI: 10.1016/j.paerosci.2012.03.004.

[31] Steijl, R. and Barakos, G. N., "Sliding mesh algorithm for CFD analysis of helicopter rotor-fuselage aerodynamics," *International Journal for Numerical Methods in Fluids 2008*, Vol. 58, No. 5, 2008, pp. 527–549, DOI: 10.1002/d.1757.

[32] Steijl, R., Barakos, G. N., and Badcock, K., "A framework for CFD analysis of helicopter rotors in hover and forward flight," *International Journal for Numerical Methods in Fluids 2006*, Vol. 51, No. 8, 2006, pp. 819–847, DOI: 10.1002/d.1086.

[33] Hirt, C. W., Amsten, A. A., and Cook, J. L., "An Arbitrary Lagrangian-Eulerian Computing Method for All Flow Speeds," *Journal of Computational Physics*, Vol. 14, No. 3, 1974, pp. 227–253, DOI: 10.1016/0021-9991(74)90051-5.

[34] Osher, S. and Chakravarthy, S., "Upwind Schemes and Boundary Conditions with Applications to Euler Equations in General Geometries," *Journal of Computational Physics*, Vol. 50, No. 3, 1983, pp. 447–481, DOI: 10.1016/0021-9991(83)90106-7.

[35] Roe, P. L., "Approximate Riemann Solvers, Parameter Vectors, and Difference Schemes," *Journal of Computational Physics*, Vol. 43, No. 2, 1981, pp. 357–372, DOI: 10.1016/0021-9991(81)90128-5.

[36] van Leer, B., "Towards the Ultimate Conservative Difference Scheme. V. A Second-Order Sequel to Godunov's Method," *Journal of Computational Physics*, Vol. 32, No. 1, 1979, pp. 101–136, DOI: 10.1016/0021-9991(79)90145-1.

[37] van Albada, G. D., van Leer, B., and Roberts, W. W., "A Comparative Study of Computational Methods in Cosmic Gas Dynamics," *Astronomy and Astrophysics*, Vol. 108, No. 1, 1982, pp. 76–84.

[38] Axelsson, O., *Iterative Solution Methods*, Cambridge University Press, 1994.

[39] Menter, F. R., "Two-Equation Eddy-Viscosity Turbulence Models for Engineering Applications," *AIAA Journal*, Vol. 32, No. 8, 1994, pp. 1598–1605, DOI: 10.2514/3.12149.

[40] Menter, F. R., Smirnov, P. E., Liu, T., and Avancha, R., "A One-Equation Local Correlation-Based Transition Model," *Flow Turbulence Combust*, Vol. 95, No. 4, 2015, pp. 583–619, DOI:10.1007/s10494-015-9622-4.

[41] Menter, F., Langrtry, R., Rikki, R., Suzen, S., Huang, P., and Volker, S., "A Correlation-Based Transition Model Using Local Variables - Part I: Model Formulation." *Journal of Turbomachinery*, Vol. 128, No. 3, 2006, pp. 1598–1605.

[42] Bousman, W. G., "Aerodynamic Characteristics of SC1095 and SC1094R8 Airfoils," NASA TP–2003-212265, Dec. 2003.

[43] Brocklehurst, A., *High Resolution Method for the Aerodynamic Design of Helicopter Rotors*, Ph.D. thesis, University of Liverpool, UK, June 2013.

[44] Kocurek, J. D. and Tangler, J. L., "A Prescribed Wake Lifting Surface Hover Performance Analysis," *Journal of the American Helicopter Society*, Vol. 22, No. 1, 1977, pp. 24–35, DOI: 10.4050/JAHS.22.24.

[45] Landgrebe, A. J., "The Wake Geometry of a Hovering Rotor and its Influence on Rotor Performance," *Journal of the American Helicopter Society*, Vol. 17, No. 4, 1972, pp. 3–15, DOI: 10.4050/JAHS.17.3.

[46] Ffowcs-Williams, J. E. and Hawkings, D. L., "Sound Generation by Turbulence and Surfaces in Arbitrary Motion," *Journal of Computational Physics*, Vol. 264, No. 1, 1969, pp. 321–342, DOI: 10.1098/rsta.1969.0031.

[47] Lighthill, M. J., "On Sound Generated Aerodynamically. I. General Theory," Proceedings of the Royal Society 221A, 1952.

[48] Brentner, K. S. and Farassat, F., "Modeling aerodynamically generated sound of helicopter rotors," *Progress in Aerospace Sciences*, Vol. 39, No. 2, 2003, pp. 83–120, DOI: 10.1016/S0376-0421(02)00068-4.

[49] Gopalan, G. and Shmitz, F. H., "Far-Field Near-In Plane Harmonic Main Rotor Helicopter Impulsive Noise Reduction Possibilities," *Proceedings of the 64th Annual Forum*, AHS, Montréal, Canada, 2008, pp. 1–22.

[50] Gopalan, G. and Shmitz, F., "Understanding Far Field Near-In-Plane High Speed Harmonic Helicopter Rotor Noise in Hover: Governing Parameters and Active Acoustic Control Possibilities," *Proceedings of Specialist's Conference on Aeromechanics*, AHS, San Francisco, CA, 2008, pp. 1–23.

[51] Kusyumov, A. N., Mikhailov, S. A., Garipova, L. I., Batrakov, A. S., and Barakos, G., "Prediction of helicopter rotor noise in hover," *EPJ Web of Conferences*, Vol. 92, No. 02042, 2015, pp. 1–5, DOI: 10.1051/epjconf/20159202042.

[52] Johnson, W., "Performance and Loads Data From a Wind Tunnel Test of a Full-Scale Rotor With Four Blade Tip Planforms," NASA TM–81229, Sept. 1980.

[53] Stroub, R. H., Rabbott, J. P., and Niebanck, C. F., "Rotor Blade Tip Shape Effects on Performance and Control Loads From Full-Scale Wind Tunnel Testing," *Journal of the American Helicopter Society*, Vol. 24, No. 5, 1979, pp. 28–35, DOI: http://dx.doi.org/10.4050/JAHS.24.28.

[54] Jepson, D., Moffitt, R., Hilzinger, K., and Bissell, J., "Analysis and Correlation of Test Data from and Advanced Technology Rotor System," NASA CR–3714, Aug. 1983.

[55] Balch, D. T., "Correlation of Full Scale Wind Tunnel Test Data with Model Rotor Test Data and Theory for a Modern Helicopter Main Rotor," *Journal of the American Helicopter Society*, Vol. 24, No. 4, 1979, pp. 45–50, DOI: http://dx.doi.org/10.4050/JAHS.24.45.

[56] Shinoda, P. M., "Performance Results from a Test of an S-76 Rotor in the NASA Ames 80- by 120- Foot Wind Tunnel," *Proceedings of the 11th Applied Aerodynamics Conference*, AIAA, Monterey, CA, 1993, pp. 126–144.

[57] Shinoda, P. M., "Full-Scale S-76 Rotor Performance and Loads at Low Speeds in the NASA Ames 80-By 120-Foot Wind Tunnel," NASA TM–110379, April 1996.

[58] Hamade, K. S. and Kufeld, R. M., "Modal analysis of UH-60A instrumented rotor blades," NASA TR–4239, Aug. 1990.

[59] Monico, M. R., Reduced Weight Rotor Blades as a Result of Flap-Bending Torsion Coupling, Rensselaer Polytechnic Institute, Hartford, Connecticut, Aug. 2013.

[60] Singleton, J. D. and Yeager, W. T., "Important Scaling Parameters for Testing Model-Scale Helicopter Rotors," *Proceedings of the 20th Advanced Measurement and Ground Testing Technology Conference*, AIAA, Albuquerque, NM, 1998, pp. 1–11.

[61] Yamauchi, G. K. and Johnson, W., "Trends of Reynolds Number Effects on Two-Dimensional Airfoil Characteristics for Helicopter Rotor Analyses," NASA TM–84363, April 1983.

[62] Acree, C., "Rotor Design Options for Improving XV-15 Whirl-Flutter Stability Margins," NASA TP–2004-212262, March 2004.

[63] Maisel, M. D., Giulianetti, D. J., and Dugan, D. C., "The History of the XV-15 Tilt Rotor Research Aircraft: From Concept to Flight," NASA SP-2000-4517, Feb. 2000.

[64] Wadcock, A. J., Yamauchi, G. K., and Driver, D. M., "Skin Friction Measurements on a Hovering Full-Scale Tilt Rotor," *Journal of the American Helicopter Society*, Vol. 44, No. 4, 1999, pp. 321–319, DOI: http://dx.doi.org/10.4050/JAHS.44.312.